The behaviour of monazite from greenschist facies phyllites to anatectic gneisses: An example from the Chugach Metamorphic Complex, southern Alaska

Deta Gasser [a,*], Emilie Bruand [a,1], Daniela Rubatto [b], Kurt Stüwe [a]

[a] Department of Earth Science, University of Graz, Universitätsplatz 2, A-8010 Graz, Austria
[b] Research School of Earth Sciences, Australian National University, Canberra, ACT 0200, Australia

ARTICLE INFO

ABSTRACT

Monazite is a common accessory mineral in various metamorphic and magmatic rocks, and is widely used for U–Pb geochronology. However, linking monazite U–Pb ages with the *PT* evolution of the rock is not always straightforward. We investigated the behaviour of monazite in a metasedimentary sequence ranging from greenschist facies phyllites into upper amphibolites facies anatectic gneisses, which is exposed in the Eocene Chugach Metamorphic Complex of southern Alaska. We investigated textures, chemical compositions and U–Pb dates of monazite grains in samples of differing bulk rock composition and metamorphic grade, with particular focus on the relationship between monazite and other REE-bearing minerals such as allanite and xenotime. In the greenschist facies phyllites, detrital and metamorphic allanite is present, whereas monazite is absent. In lower amphibolites facies schists (~550–650 °C and $\geq$ 3.4 kbar), small, medium-Y monazite is wide-spread (Mnz1), indicating monazite growth prior and/or simultaneous with growth of garnet and andalusite. In anatectic gneisses, new low-Y, high-Th monazite (Mnz2) crystallised from partial melts, and a third, high-Y, low-Th monazite generation (Mnz3) formed during initial cooling and garnet resorption. U–Pb SHRIMP analysis of the second and third monazite generations yields ages of ~55–50 Ma. Monazite became unstable and was overgrown by allanite and/or allanite/epidote/apatite coronas within retrograde muscovite- and/or chlorite-bearing shear zones. This study documents polyphase, complex monazite growth and dissolution during a single, relatively short-lived metamorphic cycle.

© 2011 Elsevier B.V. Open access under CC BY-NC-ND license.

1. Introduction

Monazite is a common accessory mineral in various metamorphic and magmatic rocks, particularly in rocks of felsic compositions, and it is an important LREE carrier (e.g. Corrie and Kohn, 2008; Spear, 2010; Spear and Pyle, 2002). Monazite incorporates relatively high concentrations of U and Th, has typically low concentrations of common Pb and is highly resistant to diffusive Pb-loss, and is thus well-suited for U–Pb geochronology (e.g. Harrison et al., 2002; Parrish, 1990). However, linking monazite ages with the *PT* evolution of the host rock is not always straightforward (e.g. Vance et al., 2003).

Monazite may occur as detrital grains below or at greenschist facies, and is stable as metamorphic monazite in rocks of appropriate bulk composition up to ultra-high temperature conditions (e.g. Goncalves et al., 2004; Spear and Pyle, 2002). Numerous studies have investigated monazite stability in metasedimentary metamorphic rocks with variable whole rock composition and metamorphic

grade, and different monazite-producing reactions have been proposed (Budzyn et al., 2011; Fitzsimons et al., 2005; Foster et al., 2000; 2004; Gibson et al., 2004; Harlov and Hetherington, 2010; Janots et al., 2006, 2008, 2009; Kim et al., 2009; Kingsbury et al., 1993; Kohn and Malloy, 2004; Kohn et al., 2005; Rasmussen et al., 2006; Rubatto et al., 2001; Smith and Barreiro, 1990; Williams et al., 2007; Wing et al., 2003). These studies highlight the importance of understanding the stability of monazite and other LREE minerals (e.g. allanite, xenotime) within a particular metamorphic sequence before a meaningful interpretation of U–Pb monazite formation dates can be obtained.

In this contribution, we present the results of an investigation of monazite stability within a single-cycle, metasedimentary sequence evolving from upper greenschist facies phyllites to amphibolite facies schists into upper-amphibolite facies migmatites. The investigated sequence is exposed along the southern Alaskan margin within a Late Cretaceous to Paleocene accretionary prism and is termed the Chugach Metamorphic Complex (CMC, Hudson and Plafker, 1982; Sisson et al., 1989; Gasser et al., 2011). We describe the textural relationships of monazite in samples of differing bulk rock composition and metamorphic grade, with particular focus on the relationship of monazite to other REE-bearing minerals such as allanite and xeno-time. The composition of monazite from the two metamorphic

---

zones where monazite is stable is monitored, and U–Pb SHRIMP dates for selected monazite samples are used to constrain the age of different monazite growth events. Our study documents the complexity of monazite growth and recrystallisation during a single-cycle, relatively short-lived metamorphic event.

2. Geology of the Chugach Metamorphic Complex

The southern Alaskan margin is dominated by a large-scale, complexly deformed Cretaceous to Paleogene accretionary prism which stretches ~2200 km from Sanak Island in the west to Baranof Island in the east (the Chugach and Prince William terranes, Fig. 1a, Plafker et al., 1994). This accretionary prism mainly consists of turbiditic rocks: conglomerates, impure sandstones, marls and claystones, which are locally intercalated with mafic volcanic rocks (e.g. Bruand et al., 2011; Nielsen and Zuffa, 1982; Sample and Reid, 2003). The accretionary prism is mainly metamorphosed in phrenite–pumpellyite to greenschist facies, but it is metamorphosed to upper amphibolite facies within the Chugach Metamorphic Complex (CMC, Fig. 1b, Bruand et al., 2011; Gasser et al., 2011; Hudson and Plafker, 1982; Pavlis and Sisson, 1995; Sisson et al., 1989).

The CMC itself consists of two macroscopically different metamorphic zones: an outer schist zone composed of fine-grained biotite–quartz–plagioclase schist, which surrounds an inner gneiss zone composed of layered migmatitic gneisses (Fig. 1, Hudson and Plafker, 1982). In the following, we additionally refer to the greenschist facies phyllites outside the CMC as the phyllite zone. The distribution of these zones is highly asymmetric: there is a wide transition from phyllites into gneisses in the north and an abrupt transition from

gneisses to phyllites along ductile to brittle faults in the south (Fig. 1; Gasser et al., 2011). The mineralogy observed in the different zones varies depending on bulk rock composition and metamorphic grade. Bulk rock compositions vary from psammites to calcareous metapelites to metapelites (Bruand, 2011). In metapelitic rocks, andalusite is wide-spread in the western and northern schist zone of the CMC and cordierite occurs locally in the western gneiss zone. Sillimanite occurs in the southern schist zone and is abundant over the entire gneiss zone, but is absent in the highest-grade rocks of the gneiss zone (Bruand, 2011; Hudson and Plafker, 1982; Pavlis and Sisson, 1995, 2003; Sisson and Pavlis, 1993; Sisson et al., 1989). Garnet is usually abundant in metapelitic to calcareous metapelitic rocks in both the schist and gneiss zones, whereas K-feldspar occurs rarely in migmatites of the gneiss zone (Bruand, 2011; Sisson et al., 1989). Metamorphosed mafic rocks exposed along the southern border of the CMC contain abundant amphibole and locally garnet (Sisson et al., 2003; Bruand et al., 2011). Sisson et al. (1989) and Bruand (2011) derived *PT* conditions of 400–550 °C and <4 kbar for the phyllite zone, ~500–650 °C and ~3–7 kbar for the schist zone, and ~650–750 °C and 4–13 kbar for the gneiss zone, with the highest pressures occurring in the southern and eastern parts of the gneiss zone (Fig. 1, Table 1).

The development of the CMC occurred during a remarkably short time span. Detrital zircon within the metasediments indicates deposition after ~65–60 Ma (Gasser, 2010; Gasser et al., in press; Kochelek et al., 2011). Based on U–Pb SHRIMP dates of thin zircon overgrowths in the migmatites of the gneiss zone, peak metamorphic conditions were reached ~5 m.y. later at ~55–51 Ma virtually simultaneously at least ~300 km along-strike of the complex (Gasser et al., in press).
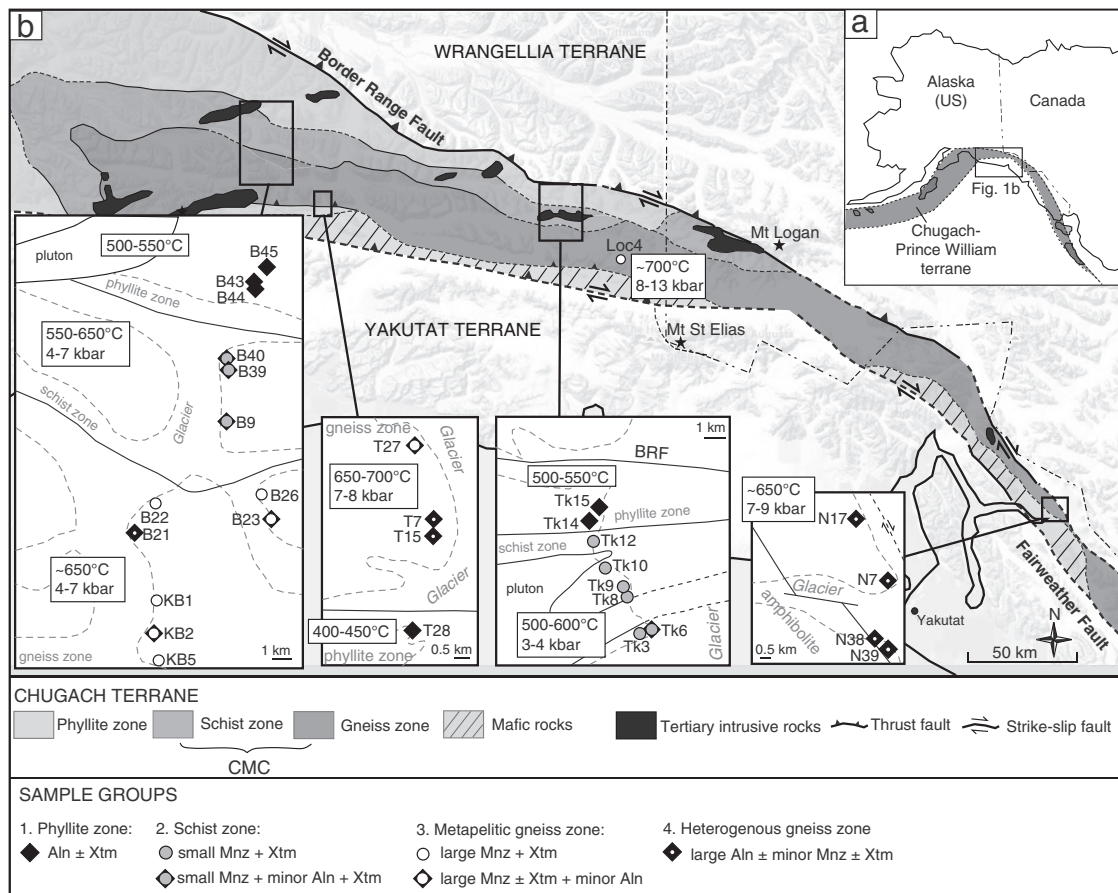
Fig. 1. (a) Overview map of Alaska and Canada with the location of Fig. 1b indicated. (b) Geological overview map of the Chugach Metamorphic Complex (CMC) within the Chugach terrane of southern Alaska. Small inset maps show stippled glacier outlines and the localities of the investigated samples as well as *PT* conditions for the different metamorphic zones after Bruand (2011). Note the location of sample Loc4 outside the small inset maps. Abbreviation: BRF = Border Range Fault System.

Table 1
List of samples and their respective mineralogy and P–T estimates.

Sample	Lat (°N)	Long (°W)	Metam. zone	Mineralogy +Qz+Pl+Bt	Mnz	Mnz(i)	Xtm	Ap	Ep/Aln	Zrn	Ilm	Ttn	Py	Hem	Rt	T(°C)[a]	p (kbar)[a]
B43	60.9263	143.2130	Phyll.	Ms–Chl–Ep			x	x	x	x	x		x	x		515±50[b]	
B44	60.9263	143.2130	Phyll.	Ms–Chl–Ep				x	x	x	x			x		535±50[b]	
B45	60.9328	143.2025	Phyll.	Ms–Chl–Ep			x	x	x	x	x		x			547±50[b]	
T28	60.6704	142.9123	Phyll.	Ms–Chl–Ep				x	x	x	x	x	x			432±50[b]	
Tk14	60.6941	141.5803	Phyll.	Ms–Chl–Ep				x	x	x	x					536±50[b]	
Tk15	60.6965	141.5739	Phyll.	Ms–Chl–Ep				x	x	x	x			x		526±50[b]	
Tk12	60.6878	141.5807	Schist	And–Ms–Grt	x		x	x		x	x					543±23[c]	3.4±0.9[c]
Tk10	60.6820	141.5716	Schist	And–Ms–Grt	x	x	x	x		x	x		x			645±49[c]	5.9±2.1[c]
Tk9	60.6752	141.5608	Schist	And–Ms–Grt	x	x	x	x		x	x		x	x		>640[b]	
Tk8	60.6731	141.5605	Schist	(And)Sil–Ms–Grt	x		x	x		x	x		x				
Tk6	60.6642	141.5488	Schist	(And)Sil–Ms	x		x	x	xr	x	x			x			
Tk3	60.6642	141.5488	Schist	(And)Sil–Ms–Grt	x	x	x	x		x	x					658±33[c]	6.4±1.4[c]
B39	60.8858	143.2384	Schist	Grt–Sil–Ms	x	x	x	x	xp?,xr	x	x		x			597±50[b]	
B40	60.8883	143.2384	Schist	Grt–Sil–Ms	x		x	x	xr	x	x		x				
B9–2	60.8583	143.2362	Schist	Grt–Sil–Ms	x		x	x	xr	x	x		x			632±30[d]	6.8±1.6[c]
B22	60.8124	143.3148	Gneiss	Grt–Sil	x		x	x		x	x		x			623±30[d]	4.7±1.9[c]
B23	60.8110	143.1928	Gneiss	Grt–Sil	x		x	x	xr	x	x	x	x			645±30[d]	
B26	60.8236	143.2033	Gneiss	Grt–Sil–Ms	x		x	x		x	x		x			628±30[d]	5.6±2[c]
KB1	60.7643	143.2881	Gneiss	Grt–Ms	x		x	x		x	x		x			645±30[d]	4.7±1.6[c]
KB2	60.7643	143.2881	Gneiss	Grt	x		x	x	xr	x	x			x		666±30[d]	5.1±1.6[c]
KB5	60.7381	143.3015	Gneiss	Ms	x		x	x		x	x		x				
T27	60.7146	142.9147	Gneiss	Grt–Ms	x		x	x	xr	x	x			x		679±32[c]	7.3±1.1[c]
Loc4	60.5544	141.3030	Gneiss	Grt–Sil–Ms	x		x	x		x	x					666±25[c]	8.2±1.2[c]
B21	60.8124	143.3148	Gneiss		x		x	x	x	x			x				
T7	60.6960	142.9031	Gneiss	Grt–Amp–Ms–Chl	xu			x	x	x	x						
T15a	60.6946	142.9069	Gneiss	Grt–Ms–Chl	x		x	x	x,xr	x	x		x	x		683±33[c]	7.3±1.1[c]
N7	59.8116	138.8131	Gneiss	Grt–Ms–Chl	xu			x	x	x	x	x	x				
N17	59.8330	138.8322	Gneiss	Grt–Ms–Chl	xu			x	x	x	x	x	x				
N38	59.7914	138.8207	Gneiss	Amp–Grt	xu			x	x	x	x		x			625±30[d]	8.3±1.2[c]
N39	59.7914	138.8207	Gneiss	Amp–Grt				x	x	x	x		x		x		

x = mineral is present in matrix, xu = mineral is unstable, Mnz(i) = monazite as inclusion in garnet and/or andalusite, xr = mineral occurs as retrograde fibres around monazite, xp = mineral is present as unstable prograde crystal. Mineral abbreviations according to Whitney and Evans, 2010
[a] PT data from Bruand (2011).
[b] Graphite thermometry.
[c] Average PT from thermocalc.
[d] Biotite–Garnet thermometry.

This short metamorphic event was followed by rapid cooling through $^{40}Ar/^{39}Ar$ muscovite and biotite closure temperatures (~480–320 °C) at 50–45 Ma in the western and central parts of the complex and slower cooling through these closure temperatures at 25–15 Ma in the southeastern part of the complex (Bradley et al., 1993; Gasser et al., 2011; Hudson et al., 1977a, 1977b, 1979; Sisson et al., 1989; Sisson et al., 2003).

3. Analytical techniques

Major element whole rock compositions of all investigated samples were obtained with a Siemens Pioneer S4 WD-XRF at the Department of Earth Sciences, University of Graz (Austria). Identification and high-contrast back-scattered electron (BSE) imaging of accessory minerals was done on polished thin sections at the Department of Earth Sciences, University of Graz (Austria) with a JEOL JSM-6310 scanning electron microscope, equipped with an IDIX EDX system for mineral identification, working at 15 kV, ~6 nA and 15 mm working distance. Element mapping and quantitative chemical analyses of monazite grains were obtained on a JEOL JXA 8200 microprobe at the Department for Applied Geosciences, University of Leoben (Austria). X-ray maps of monazite grains were obtained with 30 kV, ~10 nA, step size of ~0.2–0.4 μm and dwell times of 20–50 ms. Quantitative analyses of monazite were obtained using synthetic and natural mineral standards and a ZAF data correction scheme. Accelerating voltage was ~20 kV and beam current was 50 nA. Kα X-ray lines were used for Si, P and Ca, Lα X-ray lines were used for Y, Ce, Dy, La, Pr, Nd, Eu, Ho, Tb and Er, Lβ X-ray lines were used for Sm and Gd and Mα X-ray lines were used for Th. U and Pb were not analysed.

Monazite grains were separated for U–Pb SHRIMP dating from fist-sized samples by crushing, sieving, magnetic and heavy liquid separation, and then handpicked, mounted in epoxy and polished to expose the grain centres. BSE imaging of the separated monazite grains was done at the Electron Microscope Unit, Australian National University (ANU), with a Cambridge S360 scanning electron microscope working at 15 kV, ~2 nA and a working distance of ~17 mm. U–Pb analysis on monazite grains was performed with a sensitive high-resolution ion microprobe (SHRIMP II) at the Research School of Earth Sciences (RSES), ANU, using a beam size of ~20 μm. The data were collected in sets of six scans throughout the masses, and reference monazite 44,069 (424.9±0.4 Ma; Aleinikoff et al., 2006) was analysed each fourth analysis. Energy filtering was applied to eliminate the molecular interference on ^{204}Pb (Rubatto et al., 2001) and to reduce any matrix effect. The analyses were corrected for common Pb based on ^{204}Pb and ^{207}Pb measurements following Williams (1998). The two correction methods deliver results indistinguishable within error. Th–Pb dates, despite being less precise, are generally in agreement with the U–Pb dates. Here, ^{204}Pb corrected data are presented in Table 5 and plotted on concordia diagrams, and $^{206}Pb/^{238}U$ weighted mean dates were calculated. The common Pb composition was modelled according to Stacey and Kramers (1975). U–Pb data were collected over one analytical session using the same standard, with the session having a calibration error of 2.7% (2σ), which was propagated through to single analyses. Additionally, a 1% error was added to the final mean dates to account for external errors. Data evaluation and calculation of dates were done using the software Squid1 and Isoplot/Ex 3, respectively (Ludwig, 2003). Mineral abbreviations are according to Whitney and Evans (2010).

4. Results

In order to study the stability of monazite and other REE-bearing accessory minerals within samples of variable bulk rock composition and variable metamorphic grade across and along-strike of the Chugach Metamorphic Complex, we investigated a total of 30 samples (Fig. 1, Table 1). Sample numbers, coordinates, major and accessory minerals and *PT* conditions (Bruand, 2011) of all samples are summarised in Table 1. The major element bulk rock compositions of all samples are given in Table 2. Six samples are derived from the phyllite zone, nine samples from the schist zone, and the remaining 15 samples are from the gneiss zone of the Chugach Metamorphic Complex (Fig. 1, Table 1).

4.1. Major phase mineralogy and bulk rock compositions

The samples from the phyllite zone are composed of quartz, plagioclase, biotite, muscovite, chlorite and epidote (Table 1). All samples from the schist zone contain an aluminosilicate (andalusite and/or sillimanite), together with quartz, plagioclase, biotite, muscovite ± garnet (Table 1). The samples of the gneiss zone show variable mineralogy. There are (1) migmatitic gneisses with quartz, biotite, plagioclase, ± sillimanite, ± garnet, ± muscovite, (2) retrogressed migmatitic gneisses with wide-spread late muscovite and chlorite (T15a, N7, N17), and (3) garnet–amphibole-bearing gneisses derived from mafic volcanic rocks (T7, N38, N39; Table 1).

In general, the metasedimentary samples from all three metamorphic zones cover approximately the same range in bulk rock composition (Fig. 2, Table 2). They have compositions with Al_2O_3, Fe_2O_3 and MgO similar to average pelites (Fig. 2a; e.g. Shaw, 1956; Spear, 1993) but with generally higher CaO, Na_2O and lower K_2O values (Table 2). They probably have been derived from pelitic, marly and psammitic protoliths typical for the accretionary prism of the Chugach and Prince William terranes. Sample B40 has a considerably different composition, with very low SiO_2 but high Al_2O_3, Fe_2O_3, MgO, K_2O

and TiO_2 (Table 2). Samples N7 and B45 have relatively high SiO_2 contents. The three garnet–amphibole-bearing metavolcanic gneisses have lower SiO_2 and higher Fe_2O_3 contents than the metasedimentary samples (Table 2).

4.2. Distribution of monazite, allanite and xenotime

Depending on the occurrence of monazite, allanite and ± xenotime, the investigated samples can be classified into four different groups that broadly correspond to the metamorphic zones (Fig. 1 and Table 1).

4.2.1. Phyllite zone: allanite ± xenotime (Fig. 1, Table 1)

All samples from the phyllite zone lack monazite and contain allanite ± xenotime. Allanite occurs either as large single crystals (~20–50 μm; Fig. 3a) or as irregular small patches (~1 μm) or rims on epidote (Fig. 3b). Xenotime was observed in two of the six phyllite samples (Table 1) as very small crystals (~5–10 μm) in the matrix.

4.2.2. Schist zone: small monazite, xenotime ± minor allanite (Fig. 1, Table 1)

In the schist zone samples, monazite crystals are abundant, euhedral and small: the majority are ~5–20 μm in size with a few being ~20–50 μm in size. Most grains lie in the matrix (Fig. 3c) and some grains are associated with apatite (Fig. 3d). Monazite also occurs as inclusions in andalusite and garnet (Fig. 3e). About 70% of the grains are elongated parallel to the main foliation (regionally termed S_2, Pavlis and Sisson, 1995; Scharman et al., 2011) and some are folded by F_3 (Fig. 3c). Allanite occurs in four of the nine samples as small fibres/patches surrounding monazite and/or monazite–apatite pairs (Fig. 3f). Xenotime occurs as a minor phase in all samples, i.e. only a few crystals per thin section. The xenotime crystals are small (~5–20 μm) and occur mainly in the matrix and sometimes associated with zircon.

Table 2
Major element bulk rock compositions of all samples in weight %.

Sample	Rock[a]	SiO₂ (%)	Al₂O₃ (%)	Fe₂O₃ (%)	MnO (%)	MgO (%)	CaO (%)	Na₂O (%)	K₂O (%)	TiO₂ (%)	P₂O₅ (%)	Sum (%)
B43	p	68.86	13.35	5.76	0.07	2.39	2.06	2.20	2.04	0.70	0.15	99.44
B44	p	61.07	15.63	7.08	0.12	3.79	3.33	2.75	2.22	0.91	0.18	99.29
B45	p	70.20	13.79	5.16	0.07	1.80	1.38	1.74	2.28	0.65	0.15	99.57
T28	p	59.88	17.28	6.67	0.13	3.03	2.89	2.66	2.52	0.76	0.19	99.58
Tk14	p	66.34	12.54	6.54	0.13	3.48	4.57	2.78	1.03	0.93	0.15	99.48
Tk15	p	60.78	16.63	6.79	0.12	3.00	5.07	4.42	0.89	0.77	0.18	99.77
Tk12	s	69.22	13.77	6.02	0.09	2.15	1.43	1.91	2.25	0.68	0.18	99.60
Tk10	s	64.36	16.32	7.34	0.10	2.60	1.16	1.47	2.88	0.84	0.24	99.72
Tk9	s	69.62	12.78	6.14	0.12	2.12	1.53	1.97	2.35	0.68	0.23	99.35
Tk8	s	66.50	16.04	5.44	0.07	2.04	1.86	3.67	2.29	0.69	0.06	100.01
Tk6	s	65.59	15.74	5.74	0.08	2.31	1.06	1.97	3.30	0.74	0.18	99.87
Tk3	s	59.95	18.57	7.82	0.10	2.90	1.22	2.25	3.17	0.97	0.20	99.91
B40	s	46.54	22.30	11.60	0.22	5.30	3.58	3.47	4.01	1.22	0.09	99.92
B39	s	60.26	17.43	7.26	0.23	2.90	3.16	2.81	3.06	0.75	0.23	99.57
B9	s	60.74	17.59	7.95	0.10	3.12	1.91	2.21	3.13	0.85	0.23	100.48
B21	g	68.08	15.17	4.48	0.07	1.97	3.30	3.28	1.99	0.59	0.17	100.01
B22	g	60.36	17.89	7.27	0.11	2.86	2.79	3.27	2.93	0.84	0.25	99.60
B23	g	60.84	17.16	6.95	0.10	2.87	2.80	3.09	2.73	0.76	0.28	98.83
B26	g	63.24	16.75	7.60	0.09	3.12	2.44	2.53	2.85	0.84	0.23	100.58
KB1f	g	61.71	16.89	6.94	0.11	2.87	3.15	3.08	2.61	0.87	0.22	100.31
KB2	g	62.83	16.55	6.44	0.09	2.72	3.19	3.24	2.41	0.73	0.23	99.79
KB5rest	g	62.34	17.14	6.31	0.11	2.84	3.30	3.20	2.93	0.86	0.18	100.70
T7	mv	56.53	17.81	11.49	0.23	4.41	4.49	2.57	0.27	1.07	0.24	100.95
T15a	g	68.64	15.11	4.31	0.06	1.98	3.07	3.45	1.93	0.48	0.17	100.17
T27	g	65.88	15.43	5.31	0.09	2.25	3.19	3.12	2.21	0.61	0.31	99.65
Loc4	g	66.32	15.28	5.82	0.10	2.28	2.09	2.69	2.38	0.68	0.20	99.85
N7	g	70.94	13.29	3.58	0.10	1.52	3.56	2.89	1.29	0.49	0.14	99.29
N17	g	66.91	15.17	5.26	0.08	1.90	1.08	2.18	2.76	0.68	0.22	99.86
N38c	mv	59.53	18.04	8.01	0.23	3.12	4.07	3.35	1.83	0.84	0.20	99.93
N39	mv	57.22	16.77	12.57	0.30	3.46	4.30	1.80	1.81	0.99	0.24	100.24

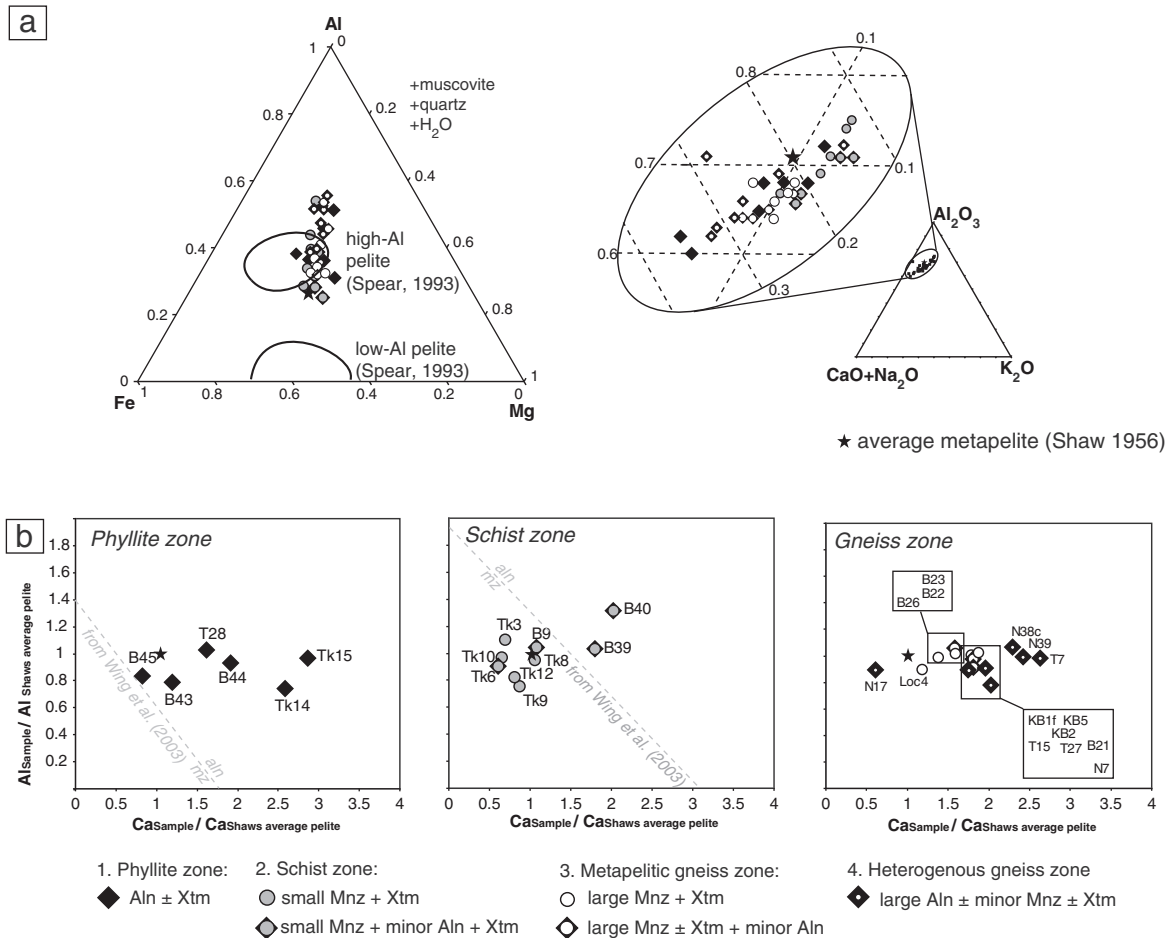[a] Rocktypes: p = phyllite, s = schist, g = gneiss, mv = metavolcanic.

Fig. 2. (a) AFM and Al_2O_3–CaO + Na_2O–K_2O diagrams for bulk rock compositions of the investigated samples. The bulk rock analyses are given in Table 2. (b) CaO vs. Al_2O_3 content of our samples relative to average metapelite of Shaw (1956). Monazite versus allanite lines according to Wing et al. (2003) for samples with *PT* conditions similar to the phyllite and schist zone samples. There is no corresponding line for samples with *PT* conditions similar to the gneiss zone samples.

4.2.3. Metapelitic gneiss zone: large monazite, xenotime ± minor allanite (Fig. 1, Table 1)

Eight samples from the gneiss zone belong to this group. They are metapelitic gneisses that lack significant retrogression and contain quartz, biotite, plagioclase, ± sillimanite, ± garnet, and ± muscovite (Table 1). Compared to the schist zone samples, the monazite grains in this group are larger (~10–100 μm, with a majority in the ~20–50 μm range) and have a sub-euhedral crystal shape. Monazite grains are located at grain boundaries or within biotite. Approximately 10% are associated with apatite (Fig. 3g). Approximately 25% of the monazite grains in three samples (B23, KB2, T27) have irregular grain boundaries and are surrounded by fine-grained allanite fibres intergrown with biotite (Fig. 3h). Xenotime is present in all samples and occurs as small crystals (~5–15 μm) in the matrix.

4.2.4. Heterogeneous gneiss zone: allanite ± xenotime ± minor monazite (Fig. 1, Table 1)

The remaining eight samples from the gneiss zone belong to this group. The group is mineralogically heterogeneous and includes a qtz + bt + pl gneiss (B21), four retrogressed gneisses with late muscovite ± chlorite (garnet-amphibole bearing sample: T7; metapelitic samples: T15, N7, N17), and two amphibole–garnet-bearing gneisses (N38, N39, Table 1). All samples contain relatively large allanite grains which locally overgrew relict monazite. In the five samples with late muscovite ± chlorite, monazite is present in the matrix as resorbed small crystals (<50 μm) with irregular grain boundaries, suggesting that these crystals represent relict grains (Fig. 3i, inset).

A few monazite grains are overgrown by allanite (Fig. 3i) or complex allanite–apatite–epidote coronas (Fig. 3j). Single, relatively large allanite crystals (100–200 μm) are present within muscovite–chlorite-bearing zones (Fig. 3k), indicating retrograde growth of allanite together with chlorite and muscovite. In sample B21, the small metastable monazite crystals are overgrown by allanite (Fig. 3l), but further indications for retrograde overprint such as muscovite and chlorite are missing in this sample. In the two amphibole-garnet bearing samples, monazite was only observed as two small (<20 μm), relict crystals in N38. Allanite is wide-spread in both samples as large and strongly zoned crystals in the matrix (~20–300 μm in size; Fig. 3m, 3n), which are commonly associated with epidote and plagioclase.

4.3. Chemical zoning and composition of monazites

Because monazite is particularly stable and common in samples from the schist zone and unretrogressed migmatites from the gneiss zone, we further investigated the chemical zoning and composition of these monazites. We conducted high-resolution BSE imaging, element mapping and quantitative chemical analyses on monazites from representative samples of these two groups.

4.3.1. Schist zone

High-contrast BSE images of all small monazite grains revealed that depending on the sample, 60–100% of the grains in each sample show no zoning, whereas the remaining 0–40% of the grains show two or three weak zones of BSE-brightness, corresponding to mass

contrasts. Grains from sample B39 that showed most variations in BSE-brightness were selected for element mapping and chemical analysis. Element X-ray maps for Y and Th show only weak variations (Fig. 4a). Representative chemical analyses from different zones of these grains are given in Table 3 and plotted in Fig. 5.

4.3.2. Gneiss zone

The large monazite grains present in the non-retrogressed migmatitic metasedimentary gneisses have more pronounced zoning than the grains from the schist zone. Up to 80% of the grains within each sample show two or more different BSE zones. Sample T27 showed well-developed zoning and was therefore selected for element X-ray mapping (Fig. 4) and chemical analysis (Fig. 5 and Table 4). The maps revealed that the strong BSE zoning is the result of inverse variations in Th and Y content, e.g. bright BSE zones correspond to high Th and low Y content. The compositional analyses show that the bright BSE zones have high but variable Th, and high La, Ce and Pr contents, whereas the dark zones have high Y, Sm, Nd, and Gd and low Th, La and Ce contents (Table 4, Fig. 5). Bright BSE zones commonly define cores and the dark zones commonly define rims (Fig. 4b). However the zoning is in many cases very patchy or mottled and no clear core-rim structure is present (Fig. 4c).
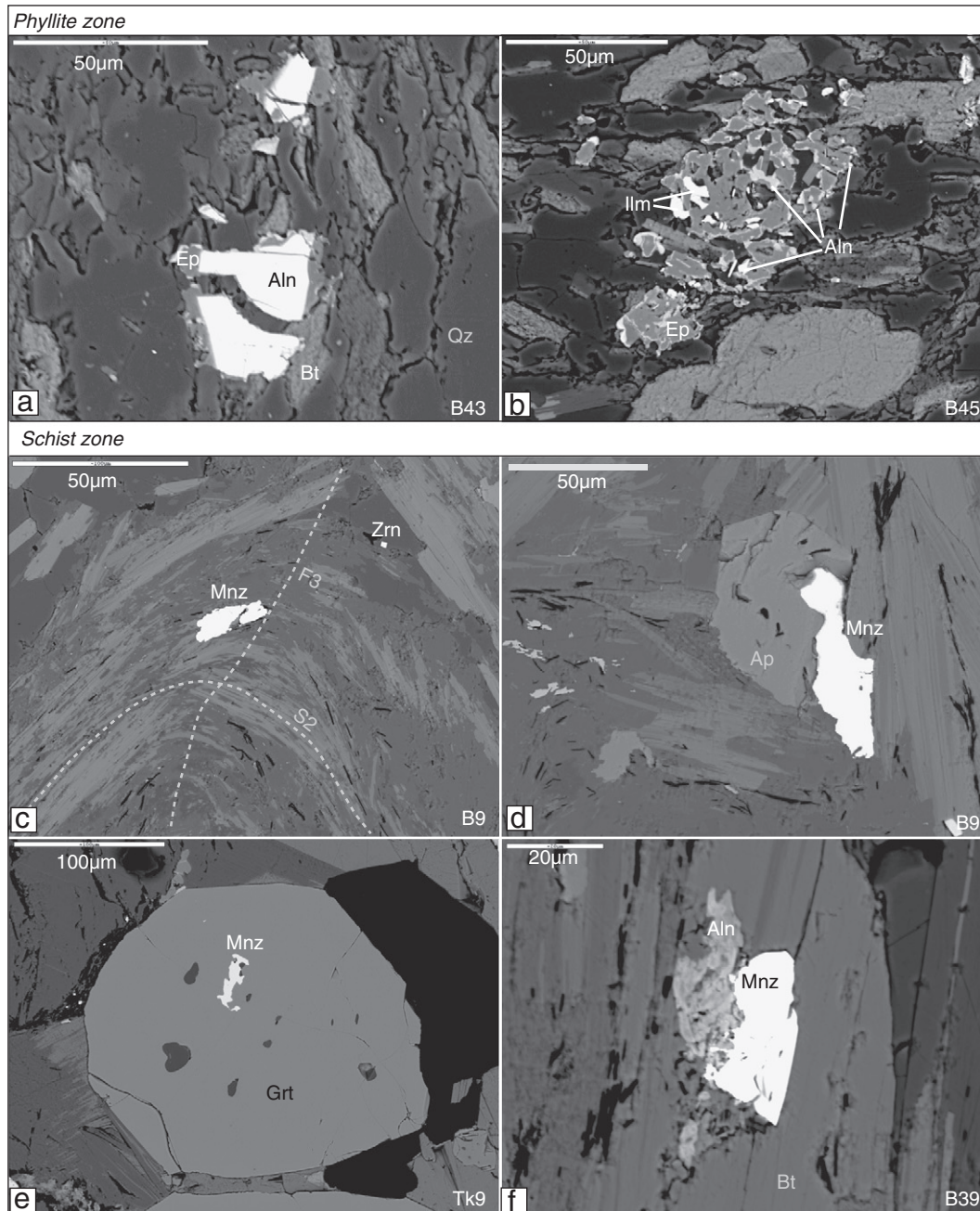

Fig. 3. BSE images of monazite and allanite occurrences within the four different sample groups identified within the CMC. In the phyllite zone, only allanite is present, either as large crystals (a) or small patches (b). In the schist zone, small monazite grains are present in the matrix (c), associated with apatite (d), in garnet or andalusite (e) and associated with allanite (f). In the migmatitic metasedimentary rocks of the gneiss zone, large monazite grains are present in the matrix (g) and are sometimes surrounded by allanite fibres (h). In retrogressed migmatitic gneisses and metavolcanic gneisses, monazite grains are generally small with a relic appearance (i, inset), and overgrown by allanite and epidote (i), or apatite + allanite + epidote coronas (j). Allanite occurs in muscovite–biotite–chlorite shear zones (k, l). Allanite occurs in the matrix of amphibole + garnet-bearing metavolcanic samples (m, n).
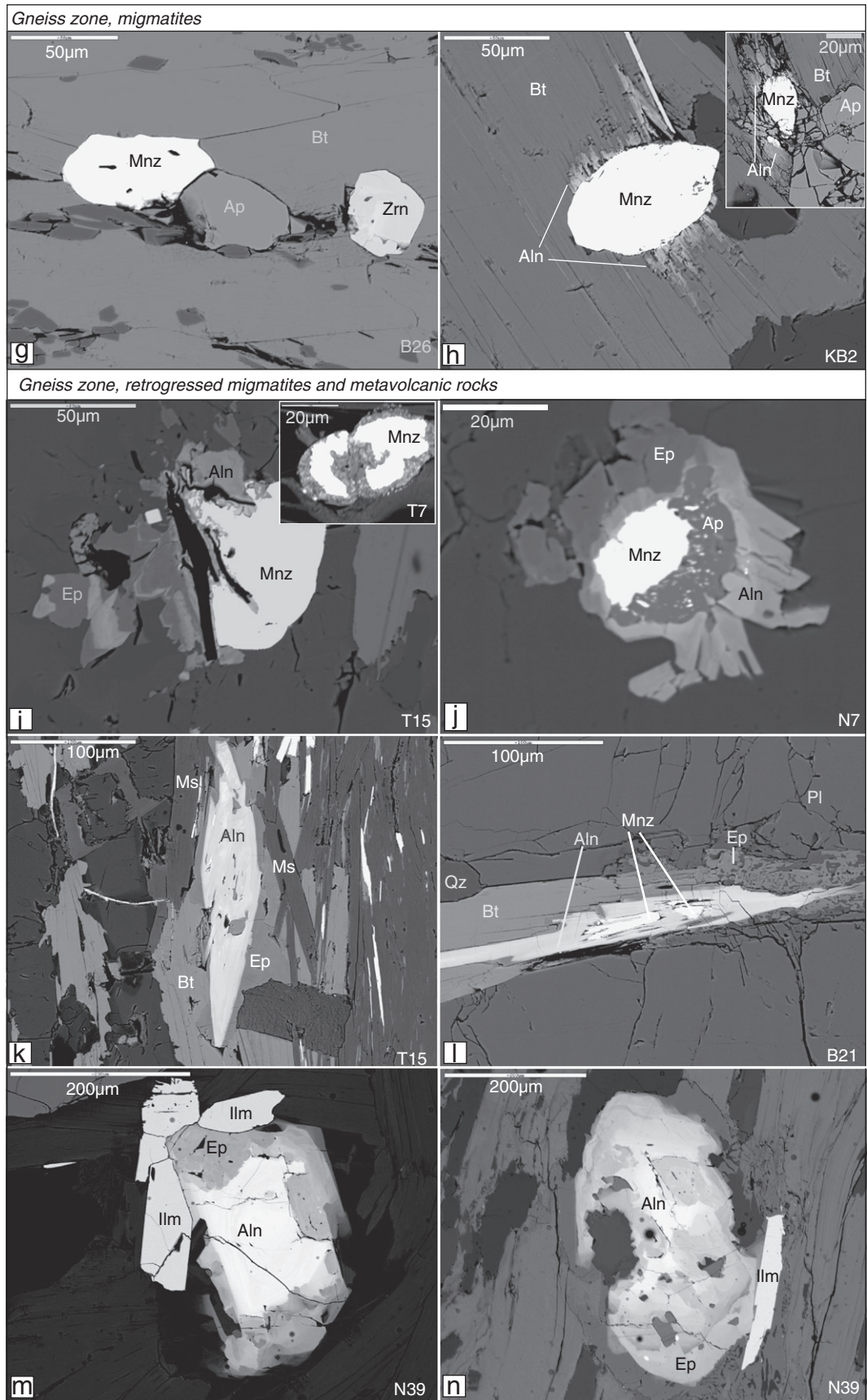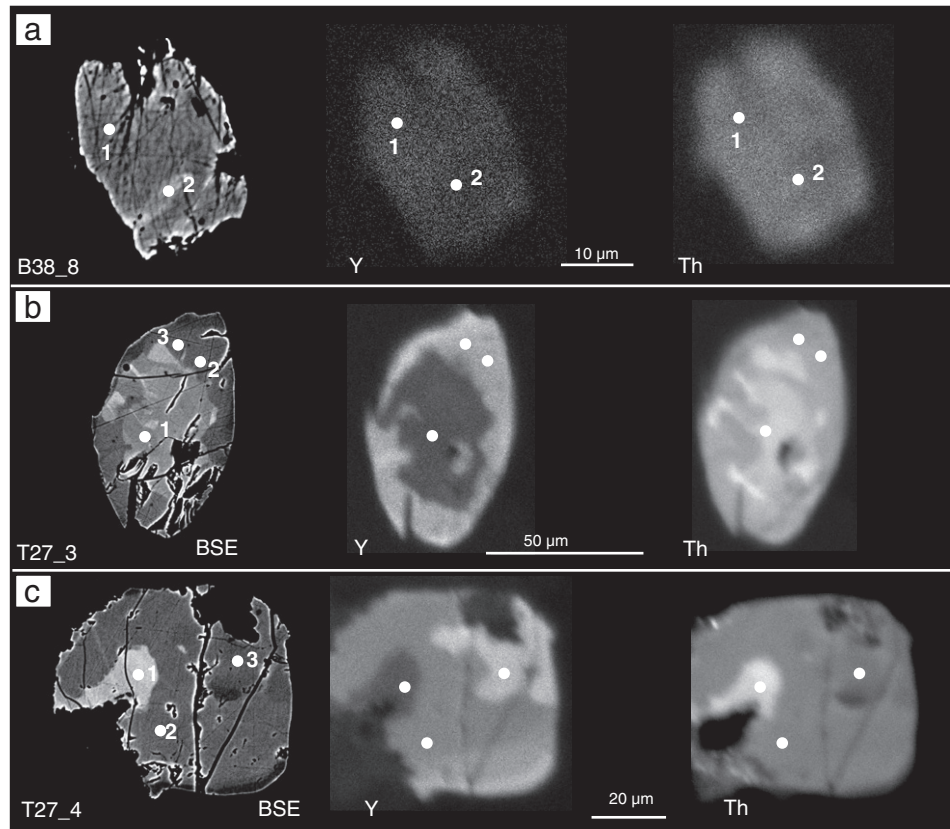
Fig. 3 (*continued*).

Fig. 4. Representative BSE images and Y and Th element maps of monazites from (a) sample B39 (schist zone, small, unzoned monazites), and (b–c) sample T27 (gneiss zone, large, complexly zoned monazites). Representative monazite EMP analyses (numbered points) are given in Tables 3 and 4.

4.4. SHRIMP U–Pb dating of monazites from the gneiss zone

Four samples from the gneiss zone that contained larger monazite grains (B21, KB5, KB1 and T27, Table 1) were selected for U–Pb SHRIMP dating. Unfortunately, an attempt of dating the small monazites from three schist samples (B39, Tk9, Tk10) was unsuccessful because mineral separation was unable to recover such small grains, and their low abundance prevented obtaining representative dates by dating them in thin section.

The four samples from the gneiss zone all yielded >50 grains of monazites per sample, typically ~50–200 μm in size. BSE images of separated grains (Fig. 6) confirm the complex zoning and the

tendency to bright BSE cores and dark BSE rims that was observed in the thin section of sample T27 (Fig. 4). We performed 13–18 analyses over 10–11 crystals from each sample covering zones with different BSE brightness (core and rims, respectively, Figs. 6 and 7). In sample KB1, one discordant analysis was excluded from the age calculation (discordant analyses are only shown in Table 5, not in Fig. 7). In sample T27, two analyses are excluded due to large errors on the isotopic ratio (Table 5). The remaining analyses from all samples form tight clusters, allowing the calculation of weighted average dates (Fig. 7). The dates vary between 51.0 ± 1.1 Ma and 53.4 ± 1.1 Ma (Fig. 7). The dates of monazite in samples KB1, KB5 and T27 are within error of each other, whereas the mean date of

Table 3
Representative monazite EMP analyses from sample B39.

	B39_1_1	B39_1_2	B39_1_3	B39_2_1	B39_2_2	B39_3_1	B39_3_2	B39_3_3	B39_8_1	B39_8_2	Min[a]	Max[a]	Av[a]
SiO_2	0.27	0.24	0.42	0.33	0.23	0.30	0.31	0.58	0.29	0.36	0.21	0.81	0.34
Y_2O_3	1.86	2.28	1.60	1.69	2.50	2.08	1.60	1.50	1.78	1.65	0.71	2.53	1.80
P_2O_5	29.92	30.03	29.95	29.65	30.04	29.63	29.64	29.44	30.02	29.62	28.60	30.10	29.70
Ce_2O_3	29.51	28.64	28.38	27.85	28.08	28.56	28.62	29.45	28.86	28.58	27.81	34.70	28.99
ThO_2	3.86	4.39	5.87	5.78	5.43	3.84	4.79	3.56	4.30	4.88	2.18	6.27	4.45
Dy_2O_3	0.21	0.34	0.26	0.57	0.54	–	0.22	0.03	0.33	0.29	–	0.59	0.33
La_2O_3	13.29	12.71	12.74	12.05	12.64	12.67	13.04	13.48	12.77	12.99	12.05	16.12	13.13
CaO	0.78	0.92	1.10	1.04	1.10	0.84	0.89	0.70	0.85	0.89	0.31	1.14	0.87
Sm_2O_3	2.12	2.18	2.10	2.46	2.08	2.08	2.14	2.19	2.21	2.33	0.98	2.46	2.12
Pr_2O_3	3.52	3.26	3.35	3.26	3.15	3.39	3.35	3.42	3.36	3.51	3.15	3.95	3.41
Gd_2O_3	1.77	1.67	1.93	2.05	1.67	1.73	1.80	1.79	1.88	1.94	0.54	2.20	1.72
Nd_2O_3	11.83	11.44	11.42	11.99	11.56	11.39	11.35	11.65	12.08	11.72	10.65	12.22	11.55
Eu_2O_3	0.74	0.72	0.76	0.84	0.76	0.61	0.82	0.74	0.71	0.78	0.61	1.15	0.77
Ho_2O_3	0.50	0.45	0.44	0.53	0.51	0.51	0.45	0.57	0.56	0.57	–	0.83	0.48
Tb_2O_3	–	0.02	–	0.01	0.05	0.06	0.12	0.04	0.08	0.02	–	0.17	0.05
Er_2O_3	–	0.02	–	–	0.08	–	–	–	–	–	–	0.12	0.02
Total	100.16	99.31	100.31	100.10	100.44	97.69	99.14	99.14	100.08	100.14	97.69	101.40	99.72

[a] Minimum, maximum and average compositions from 38 measurements on B39. All analyes are displayed in Fig. 5.

● T27 bright zones (~cores)　　　○ T27 dark BSE zones (~rims)
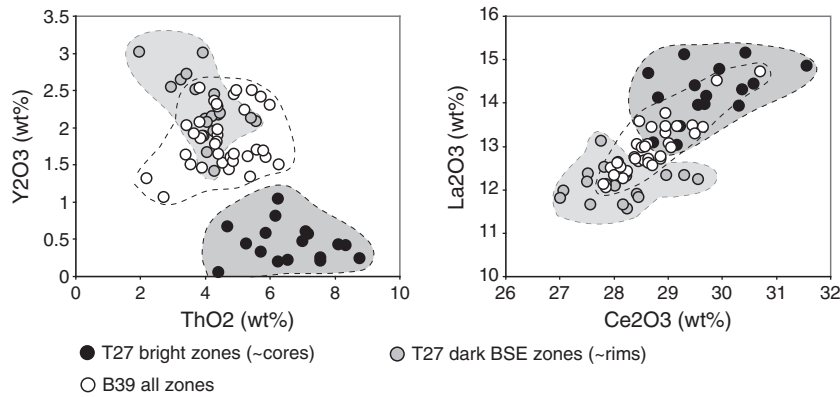
○ B39 all zones

Fig. 5. Compositional diagrams for monazite compositions analysed in samples B39 and T27. Representative EMP analyses are given in Tables 3 and 4.

monazite rims from sample B21 (51.0 ± 1.1) is slightly younger than the mean dates of monazite core and rim analyses of sample KB5, but still within error of the KB1 and T27 dates (Fig. 7). Notably, within each sample, core and rims dates are within error of each other.

5. Discussion: factors controlling monazite stability within the CMC

Based on the data on monazite distribution, chemical composition and U–Pb dates presented above, we propose and discuss a model for the behaviour of monazite in the greenschist facies phyllites to anatectic gneisses of the Chugach Metamorphic Complex (Fig. 8). We interpret our observations as the result of three key stages in the evolution of monazite: the monazite-in reaction (Mnz1), the dissolution–precipitation of monazite during partial melting and subsequent cooling (Mnz2 and Mnz3), and finally the breakdown of monazite during retrogression (Fig. 8).

5.1. Monazite-in reaction at ~550 °C and ≤3.4 kbar

Within the greenschist facies phyllites, detrital (large, broken crystals, Fig. 3a) and probably metamorphic (small, patchy crystals, Fig. 3b) allanite is present (Fig. 8). At this low grade, monazite was not observed. Therefore, the small monazites present in the schist zone (Fig. 3c–f) are interpreted as entirely metamorphic, implying that a monazite-in reaction occurred at the transition from the phyllite to the schist zone (Mnz1 growth, Fig. 8). The highest-grade sample of the phyllite zone is sample B45, which recorded a peak temperature of 547 ± 50 °C (Table 1, Bruand, 2011) at pressures of

~2–3 kbar (Sisson et al., 1989). The lowest-grade sample of the schist zone in which monazite was detected is sample Tk12, which recorded a maximum temperature of 543 ± 23 °C at 3.4 ± 0.9 kbar (Table 1, Bruand, 2011). The bulk rock composition of both samples is very similar, suggesting that the two samples are comparable (Table 2). Whereas sample B45 only contains quartz, plagioclase, muscovite and biotite as major phases, andalusite and garnet occur in addition in sample Tk12. These observations suggest that the monazite-in reaction occurred in these rocks at ~550 °C close to or at the andalusite- and garnet-in reactions at a pressure of ≤3.4 kbar (Fig. 8).

A monazite-in reaction associated with the andalusite- and garnet-in isograds in metamorphosed pelitic rocks has been reported by numerous workers (e.g. Janots et al., 2008; Kim et al., 2009; Kingsbury et al., 1993; Kohn and Malloy, 2004; Smith and Barreiro, 1990; Tomkins and Pattison, 2007; Wing et al., 2003) and has recently been modelled by Spear (2010). However, the exact reactions leading to monazite growth and the role of the major silicate phases versus other accessory phases during these reactions are debated. Most studies agree that the REE necessary for formation of the monazite probably come from the breakdown of allanite (e.g. Janots et al., 2008; Smith and Barreiro, 1990; Tomkins and Pattison, 2007; Wing et al., 2003). Kohn and Malloy (2004) additionally suggested that the major silicate phases (especially micas and garnet) could liberate considerable amounts of REE to produce monazite. However, Corrie and Kohn (2008) concluded that REEs liberated by major silicate phases are not sufficient and a REE-rich precursor such as allanite is required for monazite formation. In our case, only mica and no garnet is present in the phyllites, indicating that the REE necessary for monazite formation were probably derived from a REE-rich precursor

Table 4
Representative monazite EMP analyses from sample T27.

	T27_1_1	T27_1_2	T27_2_1	T27_2_2	T27_3_1	T27_3_2	T27_3_3	T27_4_1	T27_4_2	T27_4_3	Min[a]	Max[a]	Av[a]
SiO_2	0.63	0.31	0.69	0.44	0.69	0.40	0.38	0.75	0.32	0.35	0.27	0.93	0.49
Y_2O_3	0.20	2.12	0.26	2.19	0.44	2.15	2.52	0.60	1.66	3.00	0.06	3.02	1.38
P_2O_5	29.15	28.70	28.95	29.61	29.06	29.31	29.49	29.34	29.93	30.24	27.77	30.24	29.43
Ce_2O_3	30.37	28.17	29.56	27.85	30.58	28.02	28.01	28.82	29.30	27.01	27.01	31.56	28.86
ThO_2	6.25	4.00	7.55	4.46	5.26	4.21	3.70	7.10	4.05	3.94	1.97	8.76	5.28
Dy_2O_3	0.00	0.28	0.00	0.00	0.19	0.43	0.29	0.30	0.29	0.50	0.00	0.55	0.24
La_2O_3	14.31	11.66	13.96	12.13	14.43	12.10	12.09	14.11	12.34	11.80	11.57	15.15	13.11
CaO	1.00	1.05	1.14	1.09	0.90	1.07	1.02	1.17	0.94	1.10	0.83	1.41	1.08
Sm_2O_3	1.68	2.14	1.72	1.93	1.81	2.15	2.16	1.72	2.23	2.31	1.50	2.60	1.95
Pr_2O_3	3.63	3.18	3.59	3.04	3.46	3.21	3.16	3.64	3.40	3.12	3.04	3.81	3.40
Gd_2O_3	0.98	1.58	0.92	1.55	1.14	1.44	1.68	1.18	1.41	1.80	0.73	1.97	1.32
Nd_2O_3	11.05	11.93	11.58	11.87	11.87	12.58	12.77	10.94	13.02	12.32	10.53	13.55	11.92
Eu_2O_3	0.08	0.08	0.09	0.08	0.08	0.08	0.08	0.09	0.10	0.09	–	–	–
Ho_2O_3	0.17	0.58	0.21	0.37	0.29	0.50	0.59	0.20	0.40	0.60	–	0.68	0.32
Tb_2O_3	–	0.01	–	0.03	–	0.08	–	0.11	–	0.03	–	0.11	0.02
Er_2O_3	–	0.02	–	0.08	–	0.11	0.11	–	–	0.03	–	0.11	0.02
Total	99.50	95.83	100.21	96.71	100.20	97.84	98.02	100.07	99.39	98.23	95.17	100.95	98.90

[a] Minimum, maximum and average compositions from 35 measurements on T27. All measurements are plotted in Fig. 5.
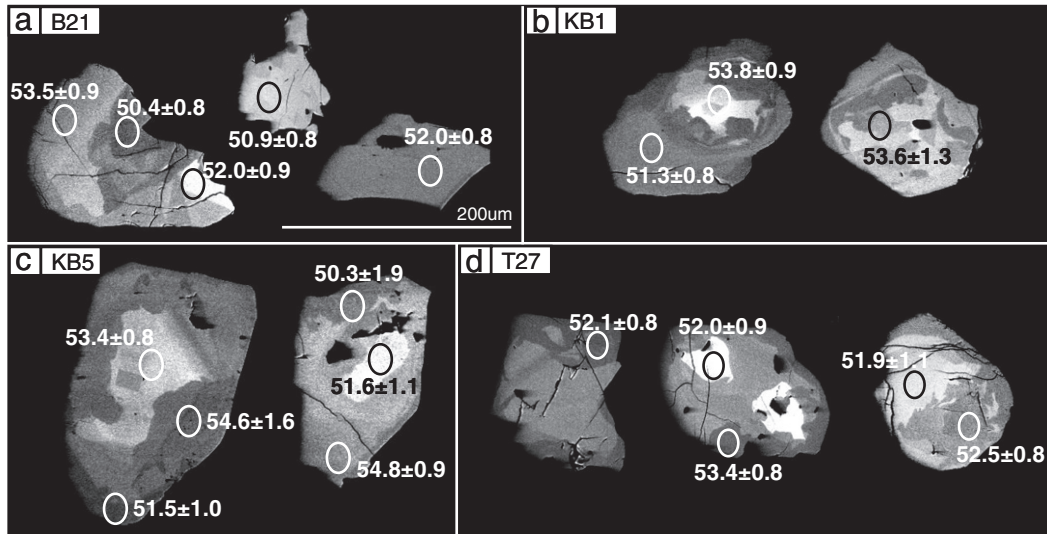
Fig. 6. Representative BSE images of dated monazite grains from the four gneiss samples. The location of the SHRIMP analyses is indicated by the ellipses and the corresponding $^{206}Pb/^{238}U$ dates (in Ma $\pm 1\sigma$) are reported. The scale is the same for all grains. Note that domains with different BSE brightness do not show differences in age. Full U–Pb analyses are given in Table 5.

such as allanite and/or xenotime. However, allanite to monazite break-down textures such as described by Janots et al. (2008), Kim et al. (2009), Tomkins and Pattison (2007) or Wing et al. (2003) were not observed in our samples. This may be due to the high level of equilibration and poor preservation of prograde relics in this sequence.

Aluminosilicates have been proposed to be necessary for the formation of monazite at or close to the andalusite and garnet-isograds. Wing et al. (2003) proposed the following reaction for the formation of monazite at the aluminosilicate-in isograd: 3 allanite + 1 apatite + 1 muscovite + 4 aluminosilicate + 3 quartz = 3 monazite + 1 biotite + 8 plagioclase + 2 H_2O. However, Tomkins and Pattison (2007) observed that the monazite-in reaction in their rocks occurred slightly down temperature of the aluminosilicate-in reaction and proposed the following general formation mechanism: allanite + apatite = monazite + plagioclase + magnetite. Similarly, Janots et al. (2008) did not observe a clear link with the aluminosilicate-in reaction and proposed the following generalised prograde reaction: allanite + apatite + Al–Fe–Mg phases1 = monazite + anorthite + Al–Fe–Mg phases2 (e.g. biotite, muscovite, garnet). In the Chugach Metamorphic Complex, the rare observation of monazite inclusions in andalusite and garnet (Fig. 3e) indicates that the monazite-in reaction probably occurred before the formation of andalusite and garnet, similar to observations by Tomkins and Pattison (2007). In addition, monazite grains in sample B39 from the schist zone are relatively Y-rich (1–2.5 wt.% Y_2O_3, Fig. 5), indicating that they probably grew before garnet, which preferentially incorporates Y (e.g. Foster and Parrish, 2003). Based on these qualitative observations, we propose that probably a reaction similar to the one proposed by Janots et al. (2008) or Tomkins and Pattison (2007) was responsible for monazite formation in the schist zone samples.

Various workers have shown that the Ca-content of the bulk rock and/or of the fluid phase influence the stability of monazite (e.g. Budzyn et al., 2011; Foster and Parrish, 2003; Janots et al., 2008; Spear, 2010; Wing et al., 2003). Several indicators have been used to show this influence. Wing et al. (2003) used CaO versus Al_2O_3 plots of andalusite-, kyanite- and sillimanite-zones to show that allanite is stable instead of monazite in their samples if the bulk rock contains 2–3 times the average pelite CaO-content. For the CMC samples of similar metamorphic grade (the phyllite and schist zones, Fig. 2b) CaO versus Al_2O_3 plots do not display such a relationship (Fig. 2b). For example, samples B39 and B40, which both lie in the stability

field for allanite as defined by Wing et al. (2003), contain abundant stable monazite, and allanite is only present as retrograde fibres or as relict prograde crystals. These retrograde allanite fibres are not restricted to samples from the allanite stability field of Wing et al. (2003), but also occur in samples in the monazite stability field (Fig. 2). Foster and Parrish (2003) proposed an equation that links the temperature of monazite growth to the CaO/SiO_2-ratio of the rock. This equation gives monazite-in temperatures of ~670 °C and ~760 °C for samples B39 and B40, respectively, suggesting that allanite should instead be stable in these samples, which is not the case. Therefore, for the CMC samples, CaO versus Al_2O_3 plots or the CaO/SiO_2 ratio seem not to be the tools for revealing the Ca-influence on monazite stability. Janots et al. (2008) suggested that the CaO/Na_2O ratio of a sample might influence the breakdown of allanite to monazite between temperatures of ~500–650 °C, with allanite being stable to higher temperatures with higher CaO/Na_2O ratio. The CaO/Na_2O ratio of all our schist samples is below 1.1, which, according to Janots et al. (2008), is clearly in the field where allanite breaks down to monazite at temperatures of ~550 °C–600 °C. This is in agreement with stable monazite being present in all schist zone samples. However, since the CaO/Na_2O ratio in our samples does not vary greatly, we could not investigate whether this ratio correctly describes monazite vs allanite stabilities in our rocks.

5.2. Dissolution and precipitation of monazite during partial melting and initial cooling

The monazite-bearing samples from the gneiss zone contain abundant, large monazite grains that are much more zoned in BSE images than the monazite grains from the schist zone. Element X-ray mapping and chemical analyses from one representative sample (T27) revealed the presence of two compositional domains: Th- and LREE-rich and Y-poor domains versus Y-, MREE-rich, and Th- and LREE-poor domains (Fig. 5). The distribution of the domains is mainly patchy, with a tendency of the Th-rich, Y-poor domains constituting cores and the Th-poor, Y-rich domains constituting rims (Figs. 4 and 6). No differences in U–Pb dates were detected between the different zones (Figs. 6 and 7). Complex compositional zoning of metamorphic monazite in upper amphibolite-facies rocks and in migmatites has been reported by many workers (e.g. Berger et al., 2009; Fitzsimons et al., 1997; Foster et al., 2002, 2004; Gibson et al., 2004; Kelsey et al., 2008; Kohn et al., 2005; Pyle and Spear, 2003; Pyle et al., 2001;
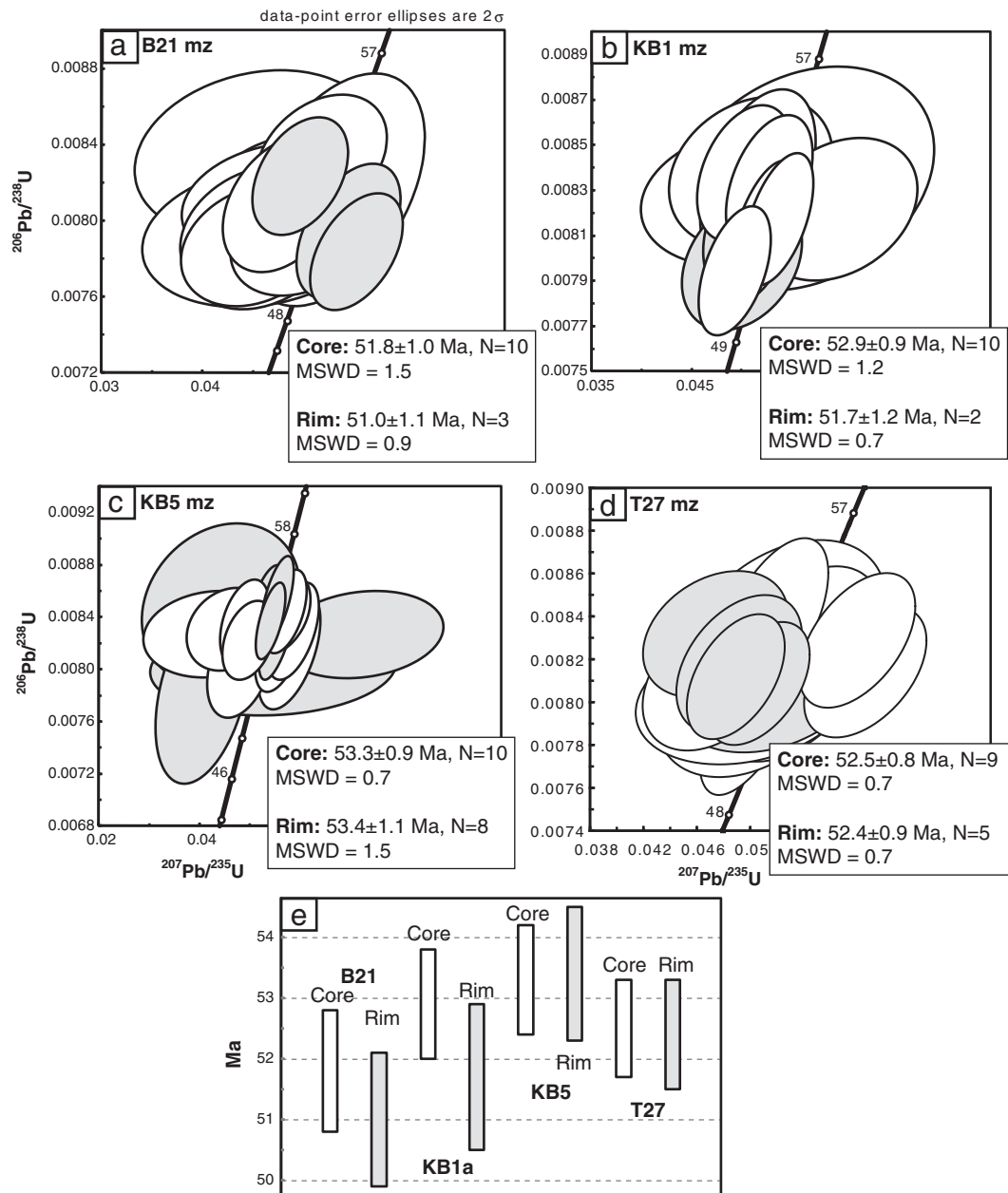
Fig. 7. (a–d) Concordia diagrams for monazites from the four gneiss samples analysed by SHRIMP. White ellipses correspond to core analyses, grey ellipses correspond to rim analyses. The values in the boxes are weighted average $^{206}Pb/^{238}U$ ages with corresponding MSWD (mean square weighted deviation). Errors are at the 95% confidence interval. N denotes number of analyses included in age calculation. Only analyses included in the age calculation are plotted (see Table 5 for the complete list of analyses). Core analyses can be correlated with monazite generation Mnz2 and rim analyses with monazite generation Mnz3 based on BSE pattern. (e) Weighted mean ages of rim and core analyses from all samples. Ages overlap within error with the only exception of monazite rims from sample B21, which are slightly younger than the ages of sample KB5.

Rubatto et al., 2001). Zoning in Y has been investigated extensively because Y is also incorporated in other phases such as garnet and xenotime (e.g. Pyle et al., 2001; Zhu and O'Nions, 1999a,b). The partitioning of Y between the different minerals may permit conclusions regarding the timing of monazite growth relative to garnet and/or xenotime growth (e.g. Pyle et al., 2001). Monazite grains in the schist zone (B39) are relatively Y-rich (Fig. 5), possibly indicating growth prior to garnet formation. Monazite grains in the gneiss zone (T27), however, show Y-poor zones preferentially in the grain cores (Fig. 4). In addition, these cores show complex zoning in Th (Fig. 4). The composition of these cores suggests that they grew when garnet was already present in the assemblage (e.g. Foster and Parrish, 2003). They could therefore represent a younger generation of monazite than the Y-rich monazite in the schist zone (Mzn2 growth, Fig. 8). This would imply that Y-rich monazite (Mnz1), which grew before

or simultaneously with garnet (i.e., monazite occurs as inclusions in garnet in the schist samples), was dissolved prior to the formation of the Y-poor monazite (Mnz2). The samples containing Mnz2 experienced partial melting under water-saturated conditions (Bruand, 2011) with garnet being stable both before and during the melting stage. Monazite solubility in metapelitic melts under water-saturated conditions can be relatively high (e.g. Montel, 1993; Rapp and Watson, 1986; Zeng et al., 2005) suggesting that dissolution of lower-grade monazite during partial melting could have occurred in the CMC. The Th-rich, Y-poor cores could then have crystallised during melt recrystallisation, with the high Th-content being the result of preferential Th incorporation into monazite in a melt-buffered system (Mnz2 growth, Fig. 8; e.g. Kohn and Malloy, 2004; Kohn et al., 2005). The recrystallisation of these large monazite grains under peak metamorphic conditions (~650–700 °C and ~4–9 kbar; Bruand,

Table 5
Monazite U–Pb shrimp data.

Label	U (ppm)	Th (ppm)	^{232}Th/^{238}U	% Pb common	^{207}Pb/^{235}U	1σ %	^{206}Pb/^{238}U	1σ %	error correlation	^{206}Pb/^{238}U Age (Ma)	±1σ
Sample B21											
B21-1C	4112	38,887	9.8	1.42	0.0474	8.2	0.00809	1.6	0.196	52.0	0.8
B21-2C	3196	26,546	8.6	0.00	0.0552	3.4	0.00784	1.6	0.469	50.4	0.8
B21-2M	5441	64,526	12.3	0.71	0.0480	5.1	0.00809	1.8	0.357	52.0	0.9
B21-2R	3080	37,389	12.5	0.37	0.0517	5.1	0.00833	1.6	0.318	53.5	0.9
B21-3C	3972	38,741	10.1	0.36	0.0497	3.9	0.00824	1.5	0.394	52.9	0.8
B21-4C	1603	23,122	14.9	1.16	0.0455	7.0	0.00795	1.8	0.253	51.0	0.9
B21-5C	2885	53,646	19.2	0.31	0.0498	5.8	0.00793	1.6	0.279	50.9	0.8
B21-6C	2626	28,878	11.4	1.03	0.0466	7.6	0.00799	2.3	0.306	51.3	1.2
B21-6R	2471	22,713	9.5	0.00	0.0545	3.9	0.00795	1.8	0.474	51.0	0.9
B21-7C	4336	39,452	9.4	0.50	0.0451	6.6	0.00787	1.7	0.250	50.6	0.8
B21-8C[a]	4943	68,740	14.4	1.35	0.0453	10.9	0.00836	2.1	0.197	53.6	1.1
B21-9C	2240	55,502	25.6	1.04	0.0457	10.4	0.00792	1.9	0.183	50.9	1.0
B21-10C	3932	29,956	7.9	0.27	0.0531	6.8	0.00817	3.0	0.446	52.4	1.6
Sample KB1											
KB1A-11R	13,417	30,504	2.3	0.18	0.0493	3.0	0.00795	1.5	0.486	51.0	0.7
KB1A-10R	6339	31,408	5.1	0.58	0.0500	4.9	0.00798	1.5	0.306	51.3	0.8
KB1A-12R	8339	32,679	4.0	0.19	0.0522	2.7	0.00813	1.5	0.567	52.2	0.8
KB1A-8C	7415	30,480	4.2	0.42	0.0511	4.0	0.00816	1.5	0.389	52.4	0.8
KB1A-6C	8198	30,578	3.9	0.00	0.0537	2.7	0.00818	1.5	0.544	52.5	0.8
KB1A-1C	5546	27,957	5.2	0.00	0.0596	5.5	0.00822	1.6	0.285	52.8	0.8
KB1A-7C	7316	32,106	4.5	0.00	0.0503	8.5	0.00827	1.5	0.177	53.1	0.8
KB1A-5C	6360	29,322	4.8	0.41	0.0527	3.4	0.00833	1.5	0.436	53.5	0.8
KB1A-3C	7383	27,492	3.8	0.42	0.0516	4.6	0.00835	2.0	0.426	53.6	1.0
KB1A-9C	2486	34,781	14.5	0.85	0.0563	9.4	0.00836	2.4	0.257	53.6	1.3
KB1A-4C	7866	28,833	3.8	0.49	0.0503	3.9	0.00838	1.5	0.374	53.8	0.8
KB1A-10C	3076	34,049	11.4	0.53	0.0509	6.6	0.00839	1.6	0.244	53.8	0.9
KB1A-2C[a]	2023	21,587	11.0	4.12	0.0199	47.6	0.00705	3.0	0.063	45.3	1.4
Sample KB5											
KB5-4C	3305	36,461	11.4	0.85	0.0479	5.6	0.00804	2.1	0.371	51.6	1.1
KB5-2C	2009	27,306	14.0	0.00	0.0577	4.4	0.00815	2.3	0.516	52.3	1.2
KB5-1C	6044	21,853	3.7	0.25	0.0560	3.7	0.00822	1.9	0.521	52.8	1.0
KB5-9C	5172	25,267	5.0	0.51	0.0496	4.3	0.00823	1.5	0.351	52.8	0.8
KB5-1OC	2688	30,811	11.8	0.00	0.0584	3.6	0.00830	1.8	0.508	53.3	1.0
KB5-1R	6867	22,129	3.3	0.00	0.0554	2.7	0.00830	1.9	0.675	53.3	1.0
KB5-8C	4537	41,541	9.5	1.13	0.0456	7.4	0.00831	1.5	0.208	53.4	0.8
KB5-7C	5012	22,550	4.6	0.52	0.0489	4.1	0.00836	1.6	0.395	53.7	0.9
KB5-1OR	10,058	18,487	1.9	0.00	0.0540	2.3	0.00838	1.4	0.635	53.8	0.8
KB5-5R	8488	20,678	2.5	0.28	0.0530	3.0	0.00843	1.8	0.590	54.1	1.0
KB5-6C	5221	38,398	7.6	0.60	0.0552	5.0	0.00844	1.6	0.314	54.2	0.8
KB5-3C	3660	31,100	8.8	0.00	0.0569	3.1	0.00845	1.6	0.499	54.2	0.8
KB5-4M	8347	20,185	2.5	0.00	0.0552	2.5	0.00853	1.6	0.652	54.8	0.9
KB5-4R[a]	4402	26,956	6.3	1.18	0.0405	9.4	0.00784	3.7	0.391	50.3	1.9
KB5-8R[a]	5323	21,729	4.2	4.42	0.0545	18.3	0.00802	1.9	0.103	51.5	1.0
KB5-2R[a]	3941	19,976	5.2	2.38	0.0721	9.2	0.00827	1.6	0.178	53.1	0.9
KB5-5C[a]	4375	37,643	8.9	1.41	0.0424	13.1	0.00828	1.6	0.124	53.1	0.9
KB5-8M[a]	2528	29,537	12.1	1.10	0.0441	14.6	0.00851	3.0	0.202	54.6	1.6
Sample T27											
T27-11C	3291	34,414	10.8	0.81	0.0497	6.8	0.00803	1.6	0.238	51.5	0.8
T27-7R	5519	31,414	5.9	0.59	0.0515	5.6	0.00808	1.6	0.280	51.8	0.8
T27-6C	4057	38,046	9.7	0.96	0.0504	6.0	0.00808	2.2	0.361	51.9	1.1
T27-10R	15,265	21,526	1.5	0.26	0.0506	3.1	0.00809	1.5	0.467	51.9	0.8
T27-1C	6439	68,741	11.0	1.13	0.0472	4.5	0.00810	1.7	0.364	52.0	0.9
T27-2R	8892	28,224	3.3	0.36	0.0489	3.1	0.00812	1.5	0.479	52.1	0.8
T27-4C	8999	22,585	2.6	0.33	0.0513	4.0	0.00814	2.9	0.709	52.2	1.5
T27-7C	3737	28,640	7.9	0.00	0.0586	3.2	0.00814	1.5	0.481	52.3	0.8
T27-9C	5246	31,195	6.1	0.80	0.0535	4.9	0.00818	2.3	0.464	52.5	1.2
T27-6R	8555	27,730	3.3	0.71	0.0492	3.9	0.00818	1.6	0.412	52.5	0.8
T27-3C	4515	36,312	8.3	0.00	0.0580	3.1	0.00829	1.6	0.507	53.2	0.8
T27-1R	9590	18,836	2.0	0.35	0.0474	4.7	0.00832	1.4	0.309	53.4	0.8
T27-8C	4677	44,039	9.7	0.46	0.0525	5.9	0.00833	2.1	0.356	53.5	1.1
T27-5C	11,855	27,660	2.4	0.38	0.0517	3.3	0.00838	1.9	0.572	53.8	1.0
T27-1M[a]	1452	44,155	31.4	1.57	0.0465	14.2	0.00759	3.9	0.275	48.8	1.9
T27-2C[a]	2796	32,899	12.2	1.50	0.0444	12.3	0.00791	2.2	0.183	50.8	1.1

[a] Denotes measurement excluded in age calculation and Concordia plots.

2011) is in agreement with experimental monazite stability fields in rocks of similar bulk composition (e.g. Janots et al., 2007). Similar monazite zoning has also been described during water-absent biotite-breakdown melting (e.g. Dumond et al., 2010).

Y-rich zones/rims similar to the Y-rich zones of sample T27 (Fig. 4) have been described by other workers from migmatitic rocks, and have generally been interpreted as representing a monazite generation which grew during breakdown of garnet and/or in
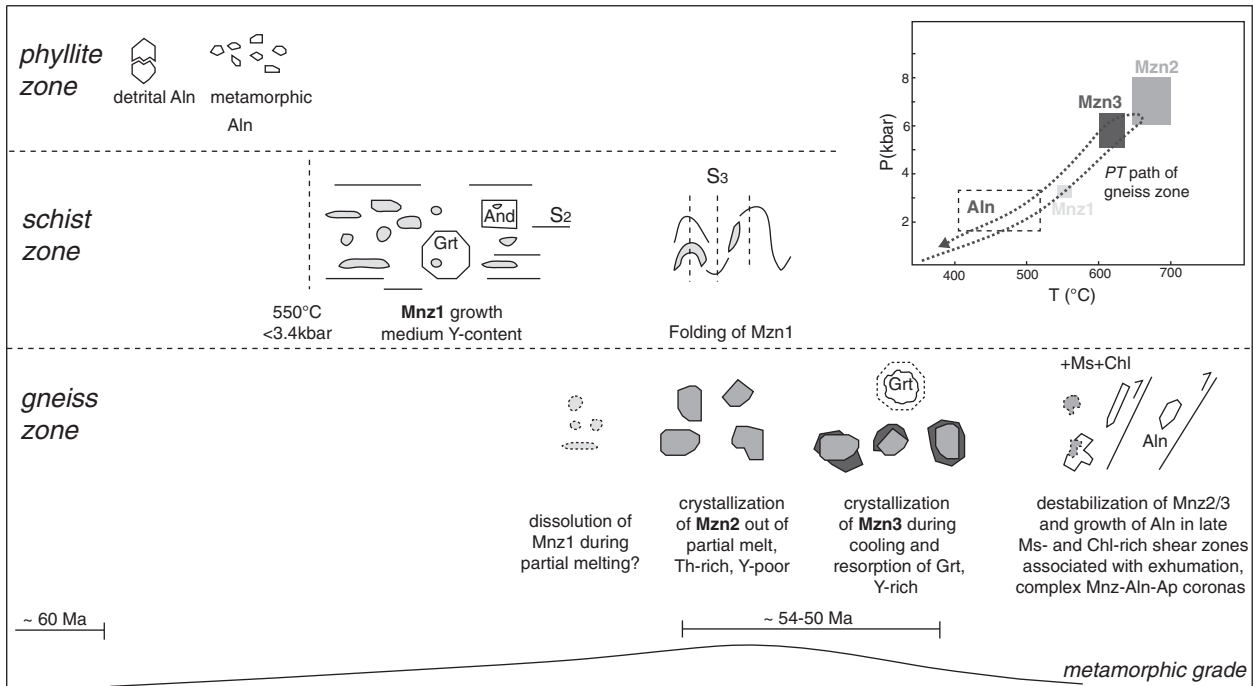
Fig. 8. Schematic diagram displaying the different stages of monazite growth and dissolution observed in the metamorphic zones of the CMC relative to metamorphic grade. In the phyllite zone, only detrital and metamorphic allanite is present. At ~550 °C and <3.4 kbar, monazite growth (Mnz1, medium Y-content) is widespread in the schist zone samples, prior to and contemporaneous with garnet and andalusite growth and parallel to the S_2 foliation. In the gneiss zone, Mnz2 growth (Th-rich, Y-poor) occurred due to recrystallisation from partial melts, and was overgrown by Mnz3 rims (Y-rich) during initial cooling and resorption of garnet. In samples located in or close to late muscovite- and chlorite-bearing shear zones, monazite was dissolved and overgrown by allanite and allanite + epidote + apatite coronas.

equilibrium with xenotime (e.g. Foster and Parrish, 2003; Kohn et al., 2005; Mahan et al., 2006; Pyle and Spear, 2003). Sample T27 contains garnet with irregular grain boundaries that show a strong outward increase in Mn and a slight decrease in Mg in the rim (Bruand, 2011). Sharp rimward zoning in Mg, Fe or Mn in otherwise homogenous garnet is commonly attributed to diffusional exchange and/or net transfer reactions between garnet and biotite during cooling (e.g. Kohn et al., 2001; Spear, 1993). Irregular grain boundaries and truncated zoning together with Mn-rich rims are commonly interpreted as resorption of garnet during which liberation of Y may occur. Additionally, dissolution of xenotime, which is indeed rare in these samples, in the final stage of melting would liberate Y. Therefore we suggest that the high-Y monazite rim (Mnz3 growth, Fig. 8) occurred after release of Y during garnet resorption and/or xenotime dissolution (e.g. Foster and Parrish, 2003; Kohn et al., 2005; Spear, 1993).

5.3. Break-down of monazite in retrograde fault zones

The retrogressed gneisses contain only small, relict monazite grains and large allanite crystals. In samples T7, T15a, N7 and N17, these allanite crystals are texturally linked to the occurrence of late muscovite and/or chlorite, which is commonly concentrated along foliation-parallel zones (Fig. 3k, Fig. 8). These muscovite–chlorite bearing zones are wide-spread in the southern and south-eastern parts of the CMC, and contain a down-dip lineation with N-side up sense of movement (Gasser et al., 2011). The zones occur near and parallel to major fault zones which bound the complex: the Contact fault system in the west and the Fairweather/Art Lewis Fault System in the south-east (Fig. 1; Gasser et al., 2011; Pavlis and Roeske, 2007; Plafker et al., 1994). These fault systems were responsible for exhumation of the CMC during the Eocene to Neogene (Gasser et al., 2011). We therefore interpret the allanite growth in these samples as a consequence of fluid-assisted greenschist facies retrogression associated with exhumation of the gneisses along the bounding

fault zones (Fig. 8). Similar allanite–apatite corona growth around monazite (as observed in samples N7 and N17, Fig. 3j) has been described by Finger et al. (1998) as a result of an amphibolite-facies overprint of granitoids and by Krenn et al. (2008) as a result of a greenschist-facies overprint of amphibolite-facies metapelites. Budzyn et al. (2011) produced similar coronas in experiments at 4.5–6.1 kbar, 450–500 °C and with high Ca-fluids, suggesting that the fluid composition plays a major role in development of such corona growth.

The two amphibole–garnet-bearing metavolcanic gneisses N38 and N39 appear to represent exceptions: the large allanite crystals present in these samples do not appear to be texturally related to the late muscovite–chlorite zones, and we infer that they represent part of the peak metamorphic assemblage. Allanite, plagioclase and garnet in these samples show complex zoning patterns in Ca, suggesting a complicated reaction history for this assemblage within these samples. The high molar Ca-content of these samples (~5 Ca mol%) relative to the other investigated samples (~1–3.8 Ca mol%), probably in combination with slightly higher overall peak pressures in the south-eastern part of the CMC (e.g. pressure controls the monazite- vs. epidote/allanite-stability field as depicted in Fig. 6 in Janots et al., 2007), likely favoured stability of allanite at the metamorphic peak in these samples.

5.4. Remarks on the U–Pb ages and regional implications

U–Pb SHRIMP dates from core and rim domains can be correlated with monazite generations Mnz2 and Mnz3, respectively, based on their similar BSE pattern (Fig. 6). Single spot analyses from rim and core domains from the different samples range from 50.3 ± 1.9 Ma to 54.8 ± 0.9 Ma (Table 5), whereas the weighted mean dates of rim and core domains of the four samples range from 51.0 ± 1.1 Ma to 53.4 ± 1.1 Ma (Fig. 7). There is no systematic difference between analyses from core and rim domains in the different samples (Fig. 7e). This indicates that Mnz2 and Mnz3 growth occurred during a short

period of time of less than 5 m.y., below the resolution of our dating method (Fig. 8). For samples KB5 and T27, U–Pb SHRIMP ages of metamorphic zircon rims are within error of the monazite ages for the same samples (54.0 ± 0.8 Ma for KB5 and 52.6 ± 0.8 Ma for T27, Gasser et al., in press). Four additional U–Pb SHRIMP ages of metamorphic zircon rims from the CMC and one age from a granodioritic intrusion also occur within error of the monazite ages (Gasser et al., in press). Metamorphic zircon rims were interpreted as being related to the partial melting event, and we suggest that monazite formation probably occurred during the same time period as the zircon-rim formation close to or at the metamorphic peak. Together, zircon and monazite ages indicate a short time period from ~55 to ~50 Ma during which partial melting occurred in the CMC, contemporaneously for at least ~300 km along strike (Gasser et al., in press).

6. Conclusions

In the Chugach Metamorphic Complex, which ranges from greenschist facies phyllites to upper amphibolites facies migmatites, monazite is affected by three major events: (1) At ca. 550 °C and ≤3.4 kbar, the detrital and metamorphic allanite present in the greenschist facies phyllites broke down to form medium-Y monazite (Mnz1). The widespread growth of monazite occurred prior to and simultaneously with garnet and andalusite growth, probably following the general reaction allanite + apatite + Al–Fe–Mg phases1 = monazite + anorthite + Al–Fe–Mg phases2. Aluminosilicates or garnet probably did not take part in the monazite-forming reaction, similarly to what has been described by Janots et al. (2008) and Tomkins and Pattison (2007). CaO versus Al_2O_3 plots, CaO/SiO_2 and CaO/Na_2O ratios do not reveal the influence of Ca on the monazite-in reaction in our samples. (2) During partial melting of the gneisses, the early medium-Y monazite generation Mnz1 was apparently dissolved, and a second, Y-poor, Th-rich monazite generation Mnz2 crystallised, which we interpret to have formed synchronous with or shortly after the metamorphic peak of ~650–700 °C and 4–9 kbar. During initial cooling and resorption of garnet rims, a third, Y-rich, Th-poor monazite generation Mnz3 formed. U–Pb SHRIMP dating of the second and third monazite generations in the gneisses shows that Mnz2 and Mnz3 are indistinguishable in age, and that the two monazite generations crystallised during a short time span of ≤5 m.y. at ~55–50 Ma. (3) Retrogression associated with the development of muscovite- and/or chlorite-bearing shear zones destabilised monazite and led to the formation of allanite and/or allanite + epidote + apatite coronas. The combination of microstructural observations, petrology, trace element geochemistry and geochronology allowed different monazite generations to be related to different metamorphic stages. The results illustrate that polyphase, complex monazite growth and dissolution can occur during a single, relatively short-lived metamorphic cycle.

Acknowledgements

References

Aleinikoff, J.N., Schenck, W.S., Plank, M.O., Srogi, L., Fanning, C.M., Kamo, S.L., Bosbyshell, H., 2006. Deciphering igneous and metamorphic events in high-grade rocks of the Wilmington Complex, Delaware: morphology, cathodoluminescence and backscattered electron zoning, and SHRIMP U–Pb geochronology of zircon and monazite. Geolocial Society of America Bulletin 118, 39–64.

Berger, A., Rosenberg, C., Schaltegger, U., 2009. Stability and isotopic dating of monazite and allanite in partially molten rocks: examples from the Central Alps. Swiss Journal of Geosciences 102, 15–29.

Bradley, D.C., Haeussler, P.J., Kusky, T.M., 1993. Timing of Early Tertiary ridge subduction in southern Alaska. In: Dusel-Bacon, C., Till, A.B. (Eds.), Geologic studies in Alaska by the U.S. Geological Survey, 1992: U.S. Geological Survey Bulletin, v. 2068, pp. 163–177.

Bruand, E., 2011. A petrological study of the Chugach Metamorphic Complex in southern Alaska. PhD thesis, Department Of Earth Sciences, University of Graz, Graz, Austria, 204 pp.

Bruand, E., Gasser, D., Bonnant, P., Stuewe, K., 2011. The petrology and geochemistry of a metabasite belt along the southern margin of Alaska. Lithos 127, 282–297.

Budzyn, B., Harlov, D.E., Williams, M.L., Jercinovic, M.J., 2011. Experimental determination of stability relations between monazite, fluorapatite, allanite, and REE-epidote as a function of pressure, temperature, and fluid composition. American Mineralogist 96, 1547–1567.

Corrie, S.L., Kohn, M.J., 2008. Trace-element distributions in silicates during prograde metamorphic reactions: implications for monazite formation. Journal of Metamorphic Geology 26, 451–464.

Dumond, G., Goncalves, P., Williams, M.L., Jercinovic, M.J., 2010. Subhorizontal fabric in exhumed continental lower crust and implications for lower crustal flow: Athabasca granulite terrane, western Canadian Shield. Tectonics 29. doi:10.1029/2009TC002514.

Finger, F., Broska, I., Roberts, M.P., Schermaier, A., 1998. Replacement of primary monazite by apatite–allanite–epidote coronas in an amphibolite facies granite gneiss from the eastern Alps. American Mineralogist 83, 248–258.

Fitzsimons, I.C.W., Kinny, P.D., Harley, S.L., 1997. Two stages of zircon and monazite growth in anatectic leucogneiss: SHRIMP constraints on the duration and intensity of Pan-African metamorphism in Prydz Bay, East Antarctica. Terra Nova 9, 47–51.

Fitzsimons, I.C.W., Kinny, P.D., Wetherley, S., Hollingsworth, D.A., 2005. Bulk chemical control on metamorphic monazite growth in pelitic schists and implications for U–Pb age data. Journal of Metamorphic Geology 23, 261–277.

Foster, G., Parrish, R.R., 2003. Metamorphic monazite and the generation of P–T–t paths. In: Vance, D., Müller, W., Villa, I.M. (Eds.), Geochronology: Linking the Isotopic record with Petrology and Textures: Geological Society of London Special Publication, 220, pp. 25–47.

Foster, G., Kinny, P., Vance, D., Prince, Ch., Harris, N., 2000. The significance of monazite U–Th–Pb age data in metamorphic assemblages; a combined study of monazite and garnet chronometry. Earth and Planetary Science Letters 181, 327–340.

Foster, G., Gibson, H.D., Parrish, R., Horstwood, M., Fraser, J., Tindle, A., 2002. Textural, chemical and isotopic insights into the nature and behaviour of metamorphic monazite. Chemical Geology 191, 183–207.

Foster, G., Parrish, R.R., Horstwood, M.S.A., Chenery, S., Pyle, J., Gibson, H.D., 2004. The generation of prograde P–T–t points and paths; a textural, compositional, and chronological study of metamorphic monazite. Earth and Planetary Science Letters 228, 125–142.

Gasser, D., 2010. Evolution of the Chugach Metamorphic Complex of southern Alaska in space and time. PhD thesis, Department Of Earth Sciences, University of Graz, Graz, Austria, 315 pp.

Gasser, D., Bruand, E., Stüwe, K., Foster, D.A., Schuster, R., Fügenschuh, B., Pavlis, T., 2011. Formation of a metamorphic complex along an obliquely convergent margin: structural and thermochronological evolution of the Chugach Metamorphic Complex, southern Alaska. Tectonics 30. doi:10.1029/2010TC002776.

Gasser, D., Rubatto, D., Bruand, E., Stuewe, K., in press. Large-scale, short-lived metamorphism, deformation and magmatism in the Chugach Metamorphic Complex (CMC), southern Alaska: a SHRIMP U–Pb study of zircons. GSA Bulletin. doi:10.1130/B30507.1.

Gibson, H.D., Carr, S.D., Brown, R.L., Hamilton, M.A., 2004. Correlation between chemical and age domains in monazite, and metamorphic reactions involving major pelitic phases: an integration of ID-TIMS and SHRIMP geochronology with Y–Th–U X-ray mapping. Chemical Geology 211, 237–260.

Goncalves, P., Nicollet, C., Montel, J.M., 2004. Petrology and in situ U–Th–Pb monazite geochronology of ultrahigh-temperature metamorphism from the Andriamena mafic unit, North–Central Madagascar. Significance of a petrographical P–T path in a polymetamorphic context. Journal of Petrology 45, 1923–1957.

Harlov, D.E., Hetherington, C.J., 2010. Partial high-grade alteration of monazite using alkali-bearing fluids: experiment and nature. American Mineralgist 95, 1105–1108.

Harrison, T.M., Catlos, E.J., Montel, J.M., 2002. U–Th–Pb dating of phosphate minerals. Reviews in Mineralogy and Geochemistry 48, 523–558.

Hudson, T., Plafker, G., 1982. Paleogene metamorphism of an accretionary flysch terrane, eastern Gulf of Alaska. Geological Society of America Bulletin 93, 1280–1290.

Hudson, T., Plafker, G., Lanphere, M.A., 1977a. Intrusive rocks of the Yakutat-St. Elias area, south-central Alaska. U.S. Geological Survey Journal of Research 5, 155–172.

Hudson, T., Plafker, G., Lanphere, M.A., 1977b. Metamorphic rocks of the Yakutat-St. Elias area, south-central Alaska. U.S. Geological Survey Journal of Research 5, 173–184.

Hudson, T., Plafker, G., Peterman, Z.E., 1979. Paleogene anatexis along the Gulf of Alaska margin. Geology 7, 573–577.

Janots, E., Negro, F., Brunet, F., Goffé, B., Engi, M., Bouybaouene, M.L., 2006. Evolution of the REE mineralogy in HP-LT metapelites of the Sebtide complex, Rif, Morocco: monazite stability and geochronology. Lithos 87, 214–234.

Janots, E., Brunet, F., Goffé, B., Poinssot, C., Burchard, M., Cemic, L., 2007. Thermochemistry of monazite-(La) and dissakite-(La): implications for monazite and allanite stability in metapelites. Contributions to Mineralogy and Petrology 154, 1–14.

Janots, E., Engi, M., Berger, A., Allaz, J., Schwarz, J.O., Spandler, C., 2008. Prograde metamorphic sequence of REE minerals in pelitic rocks of the Central Alps: implications

for allanite–monazite–xenotime phase relations from 250 to 610 °C. Journal of Metamorphic Geology 26, 509–526.

Janots, E., Engi, M., Rubatto, D., Berger, A., Gregory, C., Rahn, M., 2009. Metamorphic rates in collisional orogeny from in situ allanite and monazite dating. Geology 37, 11–14.

Kelsey, D.E., Clark, C., Hand, M., 2008. Thermobarometric modelling of zircon and monazite growth in melt-bearing systems: examples using model metapelitic and metapsammitic granulites. Journal of Metamorphic Geology 26, 199–212.

Kim, Y., Yi, K., Cho, M., 2009. Parageneses and Th–U distributions among allanite, monazite, and xenotime in Barrovian-type metapelites, Imjingang belt, central Korea. American Mineralogist 94, 430–438.

Kingsbury, J.A., Miller, C.F., Wooden, J.L., Harrison, T.M., 1993. Monazite paragenesis and U–Pb systematics in rocks of the eastern Mojave desert, California, USA: implications for thermochronometry. Chemical Geology 110, 147–167.

Kochelek, E.J., Amato, J.M., Pavlis, T.L., Clift, P.D., 2011. Flysch deposition and preservation of coherent bedding in an accretionary complex: Detrital zircon ages from the Upper Cretaceous Valdez Group, Chugach Terrane, Alaska. Lithosphere 3, 265–274.

Kohn, M., Malloy, M.A., 2004. Formation of monazite via prograde metamorphic reactions among common silicates: implications for age determinations. Geochimica et Cosmochimica Acta 68, 101–113.

Kohn, M.J., Catlos, E.J., Ryerson, F.J., Harrison, T.M., 2001. Pressure–temperature–time path discontinuity in the Maine Central thrust zone, central Nepal. Geology 29, 571–574.

Kohn, M., Wieland, M.S., Parkinson, C.D., Upreti, B.N., 2005. Five generations of monazite in Langtang gneisses: implications for chronology of the Himalayan metamorphic core. Journal of Metamorphic Geology 23, 399–406.

Krenn, E., Ustaszewski, K., Finger, F., 2008. Detrital and newly formed metamorphic monazite in amphibolite-facies metapelites from the Motajica massif, Bosnia. Chemical Geology 254, 164–174.

Ludwig, K.R., 2003. Isoplot/Ex version 3.0. A geochronological toolkit for Microsoft Excel. Berkeley Geochronological Centre Special Publication, Berkeley. 70 p.

Mahan, K.H., Goncalves, P., Williams, M.L., Jercinovic, M.J., 2006. Dating metamorphic reactions and fluid flow: application to exhumation of high-P granulites in a crustal-scale shear zone, western Canadian Shield. Journal of Metamorphic Geology 24, 193–217.

Montel, J.-M., 1993. A model for monazite/melt equilibrium and application to the generation of granitic magmas. Chemical Geology 110, 127–146.

Nielsen, T.H., Zuffa, G.G., 1982. The Chugach terrane, a Cretaceous trench-fill deposit, southern Alaska. In: Laggett, J.K. (Ed.), Trench-forearc Geology: Sedimentation and Tectonics on Modern and Active Plate Margins. Blackwell Science, pp. 213–227.

Parrish, R.R., 1990. U–Pb dating of monazite and its applications to geological problems. Canadian Journal of Earth Sciences 27, 1431–1454.

Pavlis, T.L., Roeske, S.M., 2007. The Border Range Fault System. In: Ridgway, K.D., et al. (Ed.), Tectonic Growth of a Collisional Continental Margin: Crustal Evolution of southern Alaska: Geological Society of America Special Paper, 431, pp. 95–128.

Pavlis, T., Sisson, V.B., 1995. Structural history of the Chugach metamorphic complex in the Tana River region, eastern Alaska: a record of Eocene ridge subduction. Geological Society of America Bulletin 107, 1333–1355.

Pavlis, T.L., Sisson, V.B., 2003. Development of a subhorizontal decoupling horizon in a transpressional system, Chugach metamorphic complex, Alaska: evidence for rheological stratification of the crust. In: Sisson, V.B., Roeske, S.M., Pavlis, T.L. (Eds.), Geology of a transpressional orogen developed during ridge–trench interaction along the North Pacific margin: Geological Society of America Special Paper, 371, pp. 191–216.

Plafker, G., Moore, J.C., Winkler, G.R., 1994. Geology of the southern Alaska margin. In: Plafker, G., Berg, H.C. (Eds.), The geology of Alaska. : The geology of North America, v. G-1. Geological Society of America, pp. 389–449.

Pyle, J.M., Spear, F.S., 2003. Four generations of accessory-phase growth in low-pressure migmatites from SW New Hampshire. American Mineralogist 88, 338–351.

Pyle, J.M., Spear, F.S., Rudnick, R.L., McDonough, W.F., 2001. Monazite–xenotime–garnet equilibrium in metapelites and a new monazite–garnet thermometer. Journal of Petrology 42, 2083–2107.

Rapp, R.P., Watson, E.B., 1986. Monazite solubility and dissolution kinetics: implications for the thorium and light rare earth chemistry of felsic magmas. Contributions to Mineralogy and Petrology 94, 304–316.

Rasmussen, B., Muhling, J.R., Fletcher, I.R., Wingate, M.T.D., 2006. In situ SHRIMP U–Pb dating of monazite integrated with petrology and textures: does bulk composition control whether monazite forms in low-Ca pelitic rocks during amphibolite facies metamorphism? Geochimica et Cosmochimica Acta 70, 3040–3058.

Rubatto, D., Williams, I.S., Buick, I.S., 2001. Zircon and monazite response to prograde metamorphism in the Reynolds Range, central Australia. Contributions to Mineralogy and Petrology 140, 458–468.

Sample, J.C., Reid, M.R., 2003. Large-scale, latest Cretaceous uplift along the northeast Pacific Rim: evidence from sediment volume, sandstone petrography, and Nd isotopic signatures of the Kodiak Formation, Kodiak Islands, Alaska. In: Sisson, V.B., Roeske, S.M., Pavlis, T.L. (Eds.), Geology of a transpressional orogen developed during ridge–trench interaction along the North Pacific margin: Geological Society of America Special Paper, 371, pp. 51–70.

Scharman, M., Pavlis, T.L., Day, E.M., O'Driscoll, L.J., 2011. Deformation and structure in the Chugach metamorphic complex, southern Alaska: crustal architecture of a transpressional system from a down plunge section. Geosphere 7, 992–1012.

Shaw, D.M., 1956. Geochemistry of pelitic rocks. Part III: major elements and general geochemistry. Bulletin of the Geological Society of America 67, 919–934.

Sisson, V.B., Pavlis, T.L., 1993. Geologic consequences of plate reorganization: an example from the Eocene southern Alaska fore-arc. Geology 21, 913–916.

Sisson, V.B., Hollister, L.S., Onstott, T.C., 1989. Petrologic and age constraints on the origin of a low-pressure/high-temperature metamorphic complex, southern Alaska. Journal of Geophysical Research 94, 4392–4410.

Sisson, V.B., Poole, A.R., Harris, N.R., Burner, H.C., Copeland, P., Raymond, A.D., McLelland, W.C., 2003. Geochemical and geochronologic constraints for genesis of a tonalite-trondhjemite suite and associated mafic intrusive rocks in the eastern Chugach Mountains, Alaska: a record of ridge transform subduction. In: Sisson, V.B., Roeske, S.M., Pavlis, T.L. (Eds.). Geology of a transpressional orogen developed during ridge–trench interaction along the North Pacific margin: Geological Society of America Special Paper 371, 293–326.

Smith, H.A., Barreiro, B., 1990. Monazite U–Pb dating of staurolite-grade metamorphism in pelitic schists. Contributions to Mineralogy and Petrology 105, 602–615.

Spear, F.S., 1993. Metamorphic phase equilibria and pressure–temperature–time paths. Mineralogical Society of America Monograph. . 799 pp.

Spear, F.S., 2010. Monazite–allanite phase relations in metapelites. Chemical Geology 279, 55–62.

Spear, F.S., Pyle, J.M., 2002. Apatite, monazite and xenotime in metamorphic rocks. In: Kohn, M.J., Rakovan, J., Hughes, J.M. (Eds.), Phospates. Geochemical, geobiological and materials importance: Reviews in Mineralogy and Geochemistry, 48, pp. 293–335.

Stacey, J.S., Kramers, J.D., 1975. Approximation of terrestrial lead evolution by a two-stage model. Earth and Planetary Science Letters 26, 207–221.

Tomkins, H.S., Pattison, D.R.M., 2007. Accessory phase petrogenesis in relation to major phase assemblages in pelites from the Nelson contact aureole, southern British Columbia. Journal of Metamorphic Geology 25, 401–421.

Vance, D., Müller, W., Villa, I., 2003. Geochronology: linking the isotopic record with petrology and textures — an introduction. In: Vance, D., Müller, W., Villa, I. (Eds.), Geochronology: linking the isotopic record with petrology and textures: Geological Society of London Special Publication, 220, pp. 1–24.

Whitney, D.L., Evans, B.W., 2010. Abbreviation for names of rock-forming minerals. American Mineralogist 95, 185–187.

Williams, I.S., 1998. U–Th–Pb geochronology by ion microprobe. In: McKibben, M.A., Shanks, W.C., Ridley, W.I. (Eds.), Application of microanalytical techniques to understanding mineralizing processes: Reviews in Economic Geology, 7, pp. 1–35.

Williams, M.L., Jercinovic, M.J., Hetherington, J., 2007. Microprobe monazite geochronology: understanding geologic processes by integrating composition and chronology. Annual Reviews in Earth and Planetary Sciences 35, 137–175.

Wing, B.A., Ferry, J.M., Harrison, T.M., 2003. Prograde destruction and formation of monazite and allanite during contact and regional metamorphism of pelites: petrology and geochronology. Contributions to Mineralogy and Petrology 145, 228–250.

Zeng, L., Adimow, D., Saleeby, J.B., 2005. Coupling of anatectic reactions and dissolution of accessory phases and the Sr and Nd isotope systematics of anatectic melts from a metasedimentary source. Geochimica et Cosmochimica Acta 69, 3671–3682.

Zhu, X.K., O'Nions, R.K., 1999a. Zonation of monazite in metamorphic rocks and its implications for high temperature geochronology: a case study from the Lewisian terrain. Earth and Planetary Science Letters 171, 209–220.

Zhu, X.K., O'Nions, R.K., 1999b. Monazite chemical composition: some implications for monazite geochronology. Contributions to Mineralogy and Petrology 137, 351–363.